CZECH TECHNICAL
UNIVERSITY
IN PRAGUE

F3

Faculty of Electrical Engineering
Department of Control Engineering

Master's Thesis

Control system for VTOL aircraft

Bc. Jan Belák

Prague, May 2022
Supervisor: doc. Ing. Martin Hromčík, Ph.D.
Department of Control Engineering
Faculty of Electrical Engineering of the CTU in Prague

MASTER‘S THESIS ASSIGNMENT

I. Personal and study details

Student's name: **Belák Jan** Personal ID number: **474778**

Faculty / Institute: **Faculty of Electrical Engineering**

Department / Institute: **Department of Control Engineering**

Study program: **Cybernetics and Robotics**

Branch of study: **Cybernetics and Robotics**

II. Master’s thesis details

Master’s thesis title in English:

Control system for VTOL aircraft

Master’s thesis title in Czech:

Řídicí systém pro letadlo s kolmým startem

Guidelines:

The goal of the thesis is to investigate dynamics of tilt-rotor VTOL aircraft with distributed electrical propulsion and propose unified control architecture for the aircraft's entire flight envelope. The over-actuated design of most tilt-rotor aircraft requires complicated fly-by-wire systems to be controllable for human pilot. The design of unified control system will be based on combination and expansion of well established aircraft and drone control systems.
The thesis will address the following points:
1) Design of non-linear mathematical model for tilt-rotor aircraft
2) Review of existing academia/industry solutions for VTOL aircraft control
3) Design of control system for flight mode (above the airframe's stall speed)
4) Design of full fly-by-wire system, capable of controlling the aircraft in all flight modes
5) Simulation validation and sub-scale platform based flight tests

Bibliography / sources:

[1] B. L. Stevens, F. L. Lewise. N. Johnson Aircraft Control and simulation . Third edition, John Wiley & Sons, Inc. 2016
[2] Roger W. Pratt Johnson Flight Control Systems: Practical Issues in Design and Implementation. Institution of Engineering and Technology, 2000
[3] L. Bauersfeld and G. Ducard, Fused-PID Control for Tilt-Rotor VTOL Aircraft, 2020 28th Mediterranean Conference on Control and Automation (MED), 2020, pp. 703-708. doi: 10.1109/MED48518.2020.9183031.
[4] Öznalbant Z, Kavsaoğlu MŞ. Flight control and flight experiments of a tilt-propeller VTOL UAV. Transactions of the Institute of Measurement and Control. 2018;40(8):2454-2465. doi:10.1177/0142331218754618

Name and workplace of master’s thesis supervisor:

doc. Ing. Martin Hromčík, Ph.D. Department of Control Engineering FEE

Name and workplace of second master’s thesis supervisor or consultant:

Date of master’s thesis assignment: **21.01.2022** Deadline for master's thesis submission: **20.05.2022**

Assignment valid until:
by the end of summer semester 2022/2023

doc. Ing. Martin Hromčík, Ph.D.	prof. Ing. Michael Šebek, DrSc.	prof. Mgr. Petr Páta, Ph.D.
Supervisor's signature	Head of department's signature	Dean's signature

Acknowledgement / Declaration

I would like to use this opportunity to thank my supervisor doc. Ing. Martin Hromčík, Ph.D. for his advice and support during my work on this thesis.

I would also like to thank my family and friends for their support during my studies.

Last but not least, I would also like to thank all teachers for providing me with the theoretical knowledge necessary for the creation of this thesis.

I declare that the presented work was developed independently and that I have listed all sources of information used within it in accordance with the methodical instructions for observing the ethical principles in the preparation of university theses.

In Prague on 20.5.2022

.....

Abstrakt / Abstract

Tato práce představuje novou strategii řízení letadel se schopností kolmého startu, konkrétně typu Tilt-rotor. Díky využití nelineárních řídicích algorithmů je navržený systém schopen řídit letoun ve všech fázích letu, včetně vznášení se na místě a letu cestovní rychlostí.

Práce zahrnuje všechny nezbytné kroky pro návrh funkčního řídicího systému a to včetně popisu dynamiky letadla, návrhu obecné řídicí architektury, parametrizaci systému pro specifickou platformu a na závěr validaci výsledků pomocí simulací a základních letových testů.

Navržený algorithmus umožnuje pilotovi plynule přejít z visu nad zemí do běžné letové konfigurace. Využité nelineární metody řízení také kompenzují dynamiku letounu a tím umožnují efektivní využití lineárních řídicích metod, jaké jsou PID, LQG a H_∞.

Výsledné lineární chování letounu snižuje zatížení pilota na úroveň typickou pro běžná letadla využívající systémy fly-by-wire.

Klíčová slova: Dynamická inverze, Vertikální vzlet a přistání, Nelineární řízení, Exaktní linearizace, Fly-by-wire

This thesis presents a new concept of a fly-by-wire control system for tilt-rotor type aircraft, capable of vertical take-off and landing. Due to the non-linear control approach, the proposed system can control the aircraft in all flight modes, including hover and cruise.

The thesis incorporates all necessary steps of a functional control system design. That includes a description of the aircraft dynamics, introduction of general control architecture, and system parametrization for a specific testing platform. The verification is done through high-fidelity simulations and basic flight tests.

The proposed algorithm allows the pilot to seamlessly transition from hovering above the ground to cruising in the aircraft configuration. Usage of non-linear control methods also simplifies the system dynamics, allowing for efficient usage of linear controllers, such as PID, LQG, or H_∞.

The resulting linear behavior significantly reduces the pilot's workload to a level comparable to general aviation aircraft with a fly-by-wire system.

Keywords: Dynamics inversion, Vertical take-off and landing, Non-linear control, Exact linearization, Fly-by-wire

Contents /

Chapter 1
Introduction

The aircraft industry is currently producing two types of flying machines. The first type is a fixed-wing aircraft, capable of fast and efficient travel over long distances but requiring significant infrastructure in the form of large airfields. The second is the helicopter type, having much more limited range and speed but being capable of landing nearly anywhere.

After the invention of first helicopters, the goal of companies and governments was to combine their versatility with the efficiency of an aircraft to create so-called VTOL (Vertical Take-Off and Landing) aircraft. Even though some VTOL aircraft were developed, their use was mostly limited to military cases due to the high cost of development and maintenance. However, the recent developments of electric engines and batteries promise to introduce this technology into the commercial world.

1.1 VTOL aircraft types

The first attempts at VTOL date back to the cold war era. All fighter aircraft required well-maintained airfields to operate. The promise of a fighter capable of operating without it stood behind the development of the famous *Harrier jump jet* and much less successful *Lockheed XFV-1* prototype, depicted in Figure 1.1. The military VTOL design continued to develop into today's *F-35B* and *V-22 Osprey*.

Figure 1.1. Examples of Military VTOL aircraft, *Lockheed XFV-1* on the left [1], *Harrier jump* jet in the center [2] and *V-22 Osprey* on the right [2].

These planes share two design features that prevent them from being used outside the military applications. The first is the extreme complexity of their propulsion systems, and the second is difficult maneuverability. These issues seem to solve the usage of a distributed electric power train. Electric engines are simpler, lighter, and respond much faster than fuel-based ones. These features allow for distributed propulsion design with multiple electric engines. Such a system is simpler to design, build, and easier to control. Many companies and researchers used this feature to design new VTOL aircraft concepts. Examples of which are shown in Figure 1.2.

Figure 1.2. Examples of current civil VTOL aircraft prototypes, *Joby* tilt-rotor on the left [3], *Wisk* lift and thrust in center [4] and *Dufour* tilt-wing on the right [5].

Each prototype achieves VTOL differently. The most common VTOL configuration is the so-called tilt-rotors design, where propellers can tilt upwards. Another type, called lift and thrust, has different propellers for hover and cruise modes. Last but not least is the tilt-wing design that tilts the entire wing for hover. Each system has its advantages and disadvantages, but none of them can be controlled without a fly-by-wire system.

1.2 Fly-by-wire for VTOL

Typical civil VTOL aircraft use distributed propulsion system. These engines do not only provide horizontal and vertical thrust, but also control the aircraft's attitude. Therefore, the number of actuation inputs is significantly larger than for a conventional aircraft or a helicopter. Each type of VTOL architecture requires a different approach to its control system. This thesis focuses only on the tilt-rotor architecture, an example of which is *Joby S4*, shown in Figure 1.2. The design can independently tilt each propeller to transition from hover to cruise. The control inputs are then

- Electric engines, independent of each propeller
- Tilt mechanism, changing the direction of thrust for each propeller
- Propeller's pitch angle control for large aircraft
- Traditional aerodynamic surfaces

As a typical tilt-rotor has between four and eight propellers, the overall system can even have thirty control inputs. It is nearly impossible to pilot such an over-actuated system without a complicated fly-by-wire and automatic control systems. These controllers cannot be directly adopted from the current aerospace industry due to the highly non-linear dynamics during the transition from hover to cruise regime. This thesis aims to design a general automatic control system for any tilt-rotor aircraft architecture and verify the results on a sub-scale model of an aircraft.

1.3 Thesis goals

The main goals of the thesis are summarized in the following points.

- Review the existing fly-by-wire solutions of VTOL aircraft, focusing on tilt-rotors.
- Develop a non-linear mathematical model for the tilt-rotor type aircraft.
- Design of a basic control architecture for cruise regime.
- Modify the cruise control system to expand the flight envelope and allow for a smooth transition from hover to cruise
- Verify the developed fly-by-wire system using simulations and the VTOL drone model.

1.4 Outline

The work is divided into the following sections

Firstly, Chapter 2 analyzes the current state-of-the-art fly-by-wire systems for VTOL. This analysis motives the development of the tilt-rotor fly-by-wire system.

The control system development is divided into three parts. In the first stage, a theoretical model of an aircraft is developed in Chapter 3. It describes its basic design, the power train, the avionics and analyzes its possible V-η flight envelope.
This model is then used in Chapter 4 to derive a control law for a plane in flight mode. The flight mode refers to a state in which the aircraft flies faster than stall speed and behaves like a typical aircraft.
The developed system's performance is then expanded in Chapter 5. It introduces modifications, enabling VTOL and flight below stall speed. The resulting algorithm is considered a complete fly-by-wire control system for VTOL aircraft.

The theoretical development is followed by a practical implementation of the developed algorithms for a provided sub-scale VTOL drone system in Chapter 6. The chapter describes the basic parameters of the drone and the parametrization of the fly-by-wire algorithms. The implementation is then validated in Software-in-the-loop simulations in Chapter 7 and finally tested in actual flights, as described in Chapter 8.

The tests are followed by a discussion over the results in Chapter 9, where future work on this project is considered. The Chapter 10 presents a short thesis summary.

Chapter 2
State of the art for tilt-rotor flight control

Research on the VTOL systems design is currently quite popular. Papers about the design of a VTOL drone [2], description of its dynamics [6], and comparison of different VTOL architectures [7] show a renewed interest in this subject. Comparing the different designs for long-range missions indicates that the tilt-rotor and tilt-wing designs are the most efficient.

However, these types of aircraft are also the most difficult to fly. The attempts to design a fully functional control law for tilt-rotor airframe is relatively common nowadays [8], [9], [6] and [10]. The control law designs can be divided into the following three types.

2.1 Fused controllers for hover and cruise

The fusion hover and cruise-specific controllers is an example of an approach that bypasses the complexity of a controller, which would be responsible for the entire flight envelope. It achieves the results by mixing a multi-copter and traditional aircraft controllers. The systems must also be augmented by a tilt-scheduling algorithm based on the vehicle's airspeed. These three systems are then combined based on the aircraft state to provide the final commands for actuators. An example of such a design is in [8]. The overall architecture is shown in Figure 2.1.

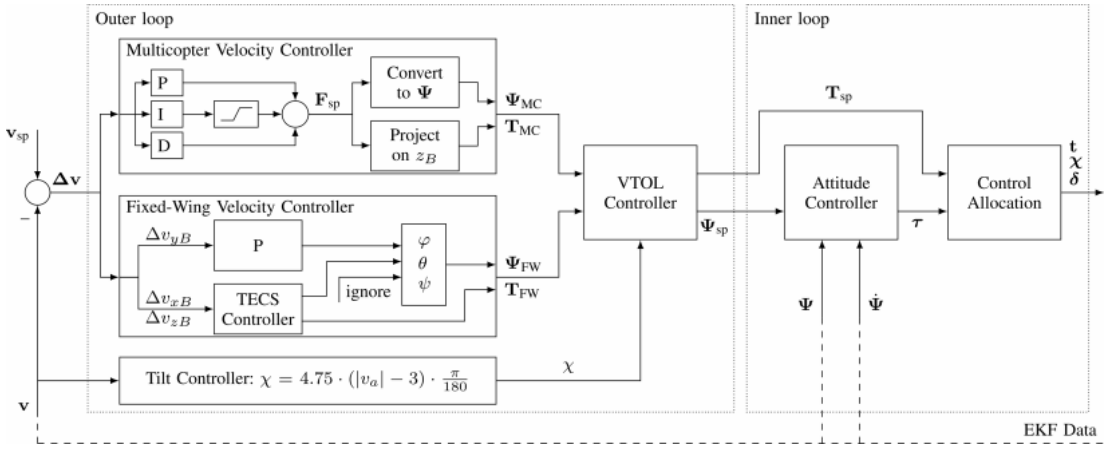

Figure 2.1. Fused PID control law for tilt-rotor system. Reproduced from [8].

Both multi-copter and traditional aircraft controllers are well described and understood. The tilt-scheduling can be done manually or through a pre-calculated trajectory based on the aircraft's state. The fusion algorithm can be represented by a gain scheduling system based on the vehicle state and the tilt angle of the propellers, as shown in [9]. The main issue with this method is ensuring robust performance in all flight scenarios. The basic control loops are designed specifically for the two flight modes. Robustness can be described well in these two modes but in no other situations. Both [8] and [9] do not mention the issue of robust design.

A modification of this approach uses torque and force commands to design the feedback loop. The torque and force commands are then used to calculate the actuator inputs. An advantage of a torque-based controller is its much simpler analysis of robustness. The method is used in [6]. However, the control allocation was not successfully described for all flight cases. The differential propeller's tilt between an aircraft's left and right sides is only considered for yaw control. This thesis will expand this technique to allow complete control allocation for the entire flight envelope.

2.2 Model predictive control (MPC)

Limitations of the previous approach can be mostly solved using optimal control theory, specifically with a model predictive control design. The MPC algorithm can either be based on linearized dynamics, evolving into solving a set of linear equations, or on non-linear dynamics, in which case the control commands are found by solving a set of non-linear differential equations. The first option is much simpler to implement, but its usage is limited by the non-linear dynamics of tilt-rotor VTOL aircraft.

The MPC can be the entire control law [10], or a high-level system, supplemented with simpler low-level controllers [11].

A common issue with the MPC-based controllers is their high computational power demands. As shown in [11], [12] or [13] the MPC approach requires a powerful flight computer, and even then, the controller's update rate is significantly lower than that of fused PID control. Moreover, the MPC does not guarantee that it will find a solution and, therefore, should be supplemented with a simpler controller for redundancy [11]. This approach is shown in Figure 2.2.

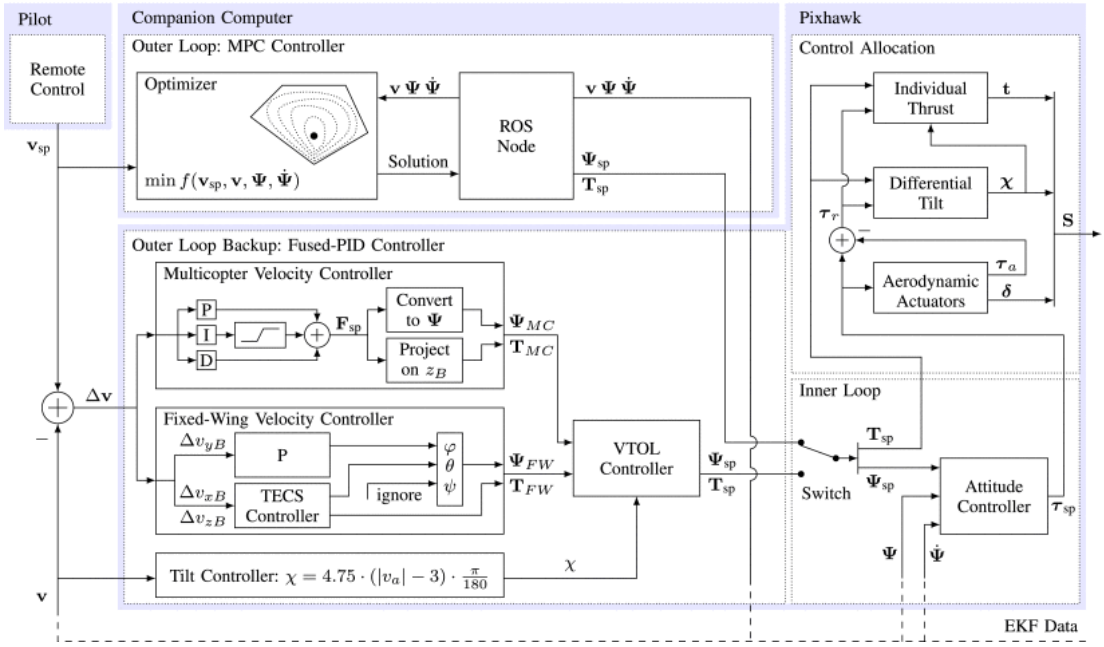

Figure 2.2. High-level model predictive controller, supplemented with fused PID for redundancy and low-level attitude controller. Reproduced from [11].

Even though the MPC-based approach shows promising results, the difficulties connected with its implementation do not seem to be fully solved for this control problem.

2.3 Feedback linearization

The last approach described in this chapter is the feedback linearization concept. These algorithms transform non-linear dynamics of the plane into virtual linearized space, where linear control algorithms can be used. The outputs of controllers are then transformed back into non-linear space to drive the system's actuators.

The algorithm combines the advantages of both previously described methods while having similar computational requirements to the fussed PID system and can be seamlessly used for the entire flight envelope like non-linear MPC. Another advantage could be the resulting linear behavior of specific aircraft states that provides the (auto)pilot with a predictive and intuitive system. Naturally, the method also has its disadvantages. The controllers require a detailed description of the system dynamics and therefore can not be tuned heuristically. This method's performance highly depends on the mathematical model's accuracy. The resulting behavior is typically sub-optimal.

Although this approach does not seem to be used to control tilt-rotor VTOL so far, it was successfully implemented for similar platforms. Such examples would be a planar VTOL [14] and a tilt-rotor drone [15]. Both of them are shown in Figure 2.3

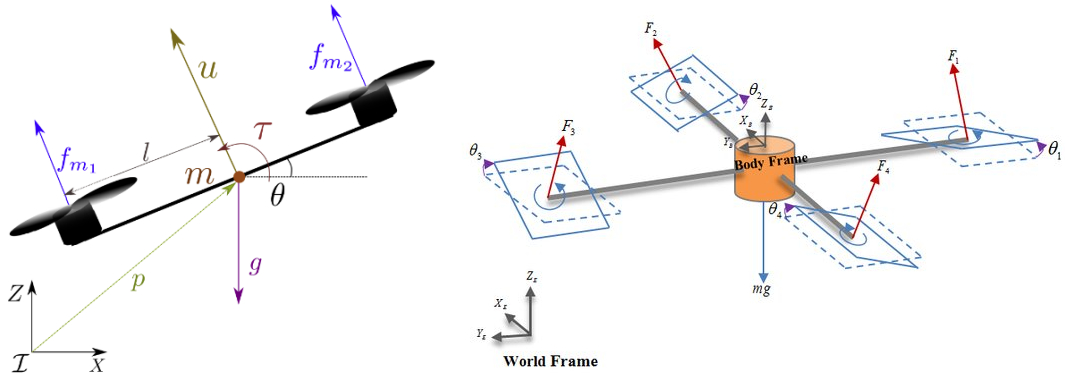

Figure 2.3. Examples of similar systems, controlled with feedback linearization. The diagram describes PVTOL system (left) and tilt-rotor drone (right). Adopted from [14] and [15].

It can be seen that both systems have similar structure and actuators as tilt-rotors. The main difference is the absence of aerodynamic surfaces and a smaller forward velocity than tilt-rotors. The primary design principles are, however, identical. Therefore the developed algorithms should be easily transferable to the tilt-rotor case.

2.4 Summary

This chapter described current state-of-the-art algorithms for the control of tilt-rotor VTOL systems. It has been shown that the research is current and significant. Also, even though several methods have already been successfully implemented, each one has its limitations and disadvantages. All available sources seem to focus on designing controllers specific to their platform with no attempts for general and transferable designs. A contribution of this thesis should be to expand the so-far-developed algorithms into more general and easily tunable systems.

Chapter 3
Mathematical model of tilt-rotor aircraft

The first step for the model-based design of a control system is to create a mathematical description of the controlled dynamics. An example of tilt-rotor aircraft is shown in Figure 3.1. The aircraft is based on a traditional monoplane design, fitted with multiple tilting propellers. Each propeller is mechanically connected to the wing or the horizontal stabilizer.

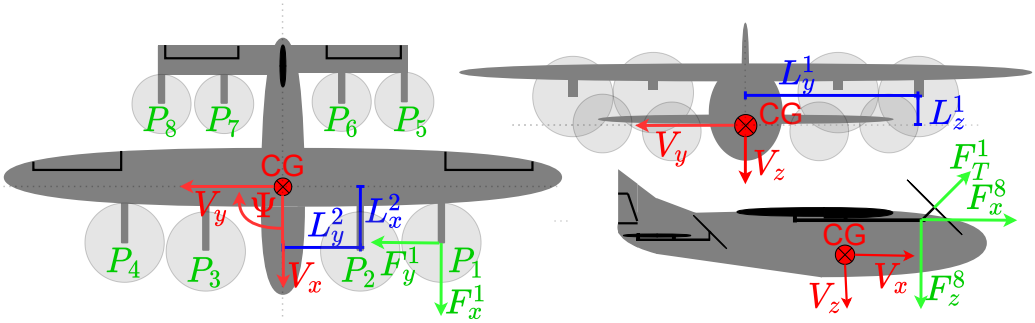

Figure 3.1. An example of tilt-rotor aircraft. The main coordinate system, centered in CG, is shown in red, the coordinate system of the propellers in green, and the distances of the propeller to CG in blue.

The description of aircraft dynamics can be highly complex. The simplest option, which still provides sufficient accuracy for control system design, divides the aircraft dynamics into the interaction between general 6DOF object, airframe aerodynamics, propellers, and suspension. Each subsystem can then be described independently. Complete aircraft dynamics are created from individual subsystems and their interaction relations.

The chapter starts by introducing the coordinate systems and variables, used in this work, in section 3.1. Then it describes the dynamics of individual subsystems in sections 3.2 through 3.5 and finally combines the dynamics in 3.6. As the complete dynamics can be considered unnecessarily complex for defining the control architecture, the dynamics are further simplified sections 3.9 for hover, 3.8 for flight, and 3.10 for transition modes.

3.1 Coordinate systems and variables.

The description uses six different coordinate systems (CS) groups, fixed to the aircraft's and an additional one to Earth's frame of reference. The mainframe CS origin is located in the plane's center of gravity (CG) and aligned with its main axes. It is followed by a free-stream CS, located at CG and aligned with the free-stream velocity vector v_∞. Then a CS for each tilt engine, based at the engine's CG and aligned with the main CS. Followed by a CS group for each propeller, placed at the propeller's center and aligned with its thrust vector. Lastly, a suspension group with one CS aligned with the Earth CS at each wheel.

Figure 3.1 shows mainframe CS and a single example of tilt engine and propeller CS. Moreover, it labels each propeller-engine CS group with the label P_i. Based on the engine and propeller, the coordinate systems have upper index e or p respectively, followed by index i, corresponding to the label P_i. An example of a suspension CS is shown in Figure 3.5. Each suspension wheel CS has an upper index wi, where i is the wheel's number.

The Earth fixed coordinate system uses North, East, Down (NED) to describe the aircraft's position.

Each CS has its own set of dynamical variables. The translation $\vec{v} = (\,V_x \quad V_y \quad V_z\,)^T$ and rotational $\vec{\omega} = (\,\omega_x \quad \omega_y \quad \omega_z\,)^T$ velocities and its derivations.

The relative position of the coordinate system with respect to the mainframe CS can be represented with the distance vector $\vec{L} = (\,L_x \quad L_y \quad L_z\,)$ and the Euler angles $\vec{E}$ (Roll Φ, Pitch Θ and Yaw Ψ).

3.2 Airframe 6DOF dynamics

The equations governing the movement of a free rigid body with six degrees of freedom in 3-dimensional space are described in [16]. The relations can be written as

$$M\dot{\vec{v}} + D\vec{v} = \vec{F}, \tag{3.1}$$

$$I_\omega\dot{\vec{\omega}} + \vec{\omega} \times (I_\omega\vec{\omega}) = \vec{M}_\omega, \tag{3.2}$$

where M is mass [kg], D is drag [N·s·m^{-1}], and I_ω is the inertia [kg·m^2] matrix. The forces $\vec{F}$ [N], torques $\vec{M}_\omega$ [N·m], rotational $\vec{\omega}$ [rad ·s^{-1}] and translation $\vec{v}$ [m·s^{-1}] velocities are 3×1 column vectors. In most flight situations, the rotation rates $\vec{\omega}$ will be close to zero. This assumption allows to emit the non-linear $\vec{\omega} \times (I_\omega\vec{\omega})$ relation from the equation (3.2) and therefore linearize the equations.

3.3 Aerodynamic forces

The aerodynamic forces are created by the interaction between the airframe and surrounding air. The lift and drag forces are generated in the free-stream CS. Angles between free-stream and the mainframe CS can be described by the angle of attack (3.3) and angle of sideslip (3.4).

$$\alpha = \arctan(\frac{v_z}{v_x}), \tag{3.3}$$

$$\beta = \arcsin(\frac{v_y}{v_\infty}), \tag{3.4}$$

where $v_\infty = \sqrt{v_x^2 + v_y^2 + v_z^2}$. The lift and drag, referenced to the free-stream air CS, depend on these angles and can be described as

$$\vec{F}^{air} = I \otimes (-P_d \cdot A) \cdot \begin{pmatrix} c_d \cdot c_l^2 \cdot \alpha^2 + c_{d0} \\ c_s \cdot \beta \\ c_l \cdot \alpha + c_{l0} \end{pmatrix}, \tag{3.5}$$

where $\otimes$ represents Kronecker product [17], $P_d = \frac{\rho v_\infty^2}{2}$ is dynamic pressure, A is the reference area and parameters c are dimensionless constants, representing the specific

airframe shape. Furthermore, the aerodynamic effect can also create a moment, acting on the airframe. The moment can be described with an equation

$$\vec{M}(\alpha, \beta, P_D) = I \otimes (P_d \cdot A \cdot b) \cdot \begin{pmatrix} c_r \cdot \beta \\ c_p \cdot c_l \cdot \alpha + c_{p0} \\ c_y \cdot \beta \end{pmatrix}, \tag{3.6}$$

where b is typically wing chord. The described interaction between the atmosphere and plane significantly simplifies the aircraft's aerodynamics. For example, the drag created by large rotational velocities of the aircraft is neglected. This simplification means that the aircraft aerodynamics are not modeled in the hover mode. Another simplification is the assumption of low values of α and β. Therefore the described system cannot correctly model maneuvers with a high angle of attack.

3.3.1 Effect of control surfaces

The so-far described aerodynamics did not consider any controllable surfaces on the aircraft. A comprehensive description of typical control surfaces is shown in Figure 3.2. These systems can be divided into two groups.

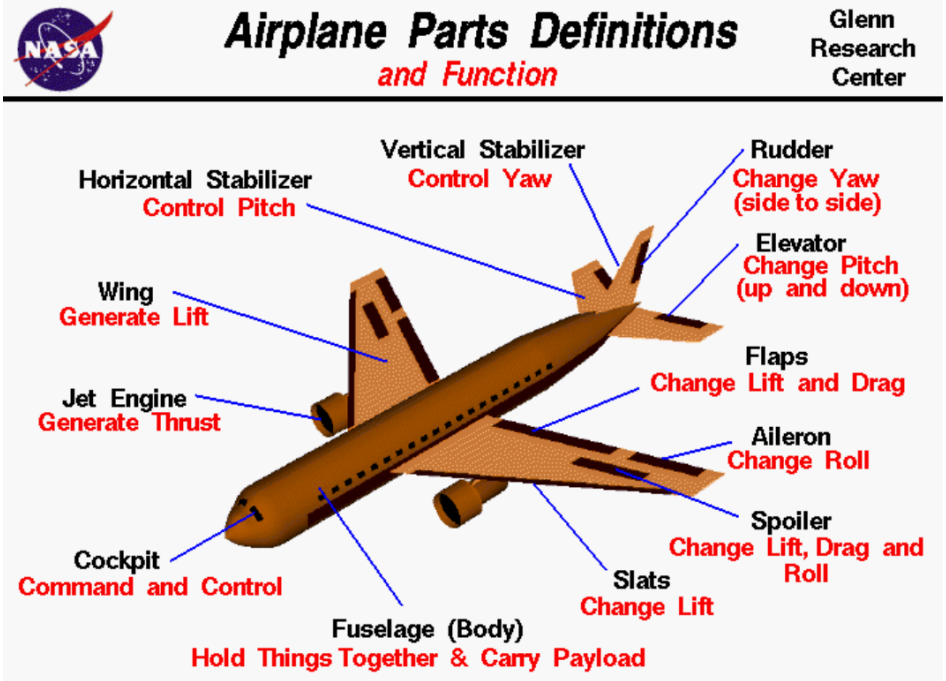

Figure 3.2. A description of aircraft control surfaces. Reproduced from [18].

The first group is only used to modify the aerodynamic coefficients of the airframe. A typical example would be the flaps that modify the lift and drag coefficients c_l and c_d. These systems usually react fairly slowly and are not used to directly control the aircraft's state. Instead, they are used to extend the flight envelope during take-off and landing. These systems will not be considered in this thesis.

The second group has a significantly faster response time and is used to control the aircraft dynamics directly. Traditional members of this group are the ailerons, rudder, and elevator. The control surfaces generate a moment on the airframe when deflected.

The relation between the deflection angle and the resulting moment can be written as

$$\Delta\vec{M}(A_L, A_R, E, R, P_D) = I \otimes (P_d \cdot A \cdot b) \cdot \begin{pmatrix} c_{ra} & -c_{ra} & 0 & 0 \\ c_{pa} & c_{pa} & c_{pe} & 0 \\ c_{ya} & -c_{ya} & 0 & c_{yr} \end{pmatrix} \begin{pmatrix} \Delta A_L \\ \Delta A_R \\ \Delta E \\ \Delta R \end{pmatrix}, \quad (3.7)$$

where c_{ra}, c_{pa}, c_{ya}, c_{pe} and c_{yr} are relevant constants. The value ΔA_R describes compensated deflection of the right aileron, ΔA_L of the left one. Elevator ΔE and rudder ΔR deflections are also present.

The moment function is expected to be linear with respect to the deflections. However, a typical aileron does not necessarily create the same moment value for positive and negative deflection. This issue can be fixed by compensating the real reflection values to achieve the same slope for positive and negative deflection changes.

3.4 Propeller and Engine system

In most cases, the tilt-rotor architecture uses propellers powered by electric engines to achieve thrust. The model describes a generation of force according to provided command. The system can be divided into propeller and engine components.

3.4.1 Propeller

The description of propeller geometry and generated forces is shown in Figure 3.3.

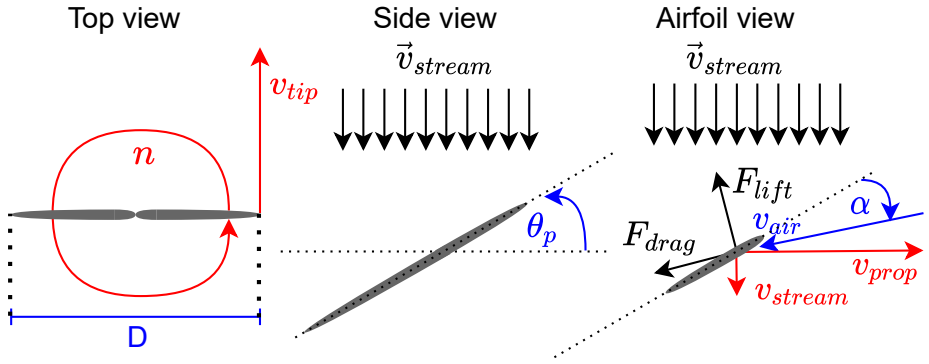

Figure 3.3. The basic geometry of a propeller.

The two considered geometric parameters are the diameter D [m] and pitch angle θ_p [rad]. The propeller spins with rotational velocity n [s^{-1}]. The resulting relative flow over airfoil v_{air} is a combination of the local propeller velocity v_{prop} and the free stream velocity v_{stream}. The airfoil generates forces according to the same equation as the wing (3.5) with the angle of attack α and an assumption of zero sideslip angle. The maximal airspeed over the airfoil is at the tip of the propeller, described as $v_{tip} = \pi \cdot n \cdot D$.

In the case of hover mode, the v_{stream} is approximately zero. Therefore the generated thrust F_T and torque Q_T depend only on the propeller rotational speed n and can be derived from (3.5) as

$$F_T \approx c_{T0}(\theta_p) \cdot n^2, \quad (3.8)$$

$$Q_T \approx c_{Q0}(\theta_p) \cdot n^2, \quad (3.9)$$

In cruise the v_{stream} is not zero. To calculate the thrust in such a situation, the introduction of the advance ratio (3.10) and the Mach speed of the propeller's tip (3.11) is needed.

$$J = \frac{v_{stream}}{n \cdot D}, \tag{3.10}$$

$$M_{tip} = \frac{v_{tip}}{a}, \tag{3.11}$$

where a is local speed of sound. These variables are used in the description of thrust (3.12), torque (3.13), input power (3.13) and efficiency (3.15) according to equations

$$F_T = c_T(J, M, \theta_p) \cdot \rho \cdot n^2 \cdot D^4, \tag{3.12}$$

$$Q_T = c_Q(J, M, \theta_p) \cdot \rho \cdot n^2 \cdot D^5, \tag{3.13}$$

$$P_{in} = c_P(J, M, \theta_p) \cdot \rho \cdot n^3 \cdot D^5, \tag{3.14}$$

$$\eta = J \cdot \frac{c_T(J, M, \theta_p)}{c_P(J, M, \theta_p),} \tag{3.15}$$

where ρ is air density. Parameters c_T, c_P and c_Q depend in general on J, M and θ_p. However, in cases, where $v_{tip} \ll a$, the dependency on M can be neglected.

Both relations (3.8), (3.9) and (3.12), (3.13) are dependent on propeller pitch θ_p. An example of parameter dependency is shown in Figure 3.4.

Variable pitch propellers can control thrust by changing the pitch and rotational velocity. This configuration requires non-linear multidimensional optimization algorithms to achieve its full potential. Moreover, most small drones do not have a variable pitch propeller. For these reasons, only fixed pitch propellers will be considered.

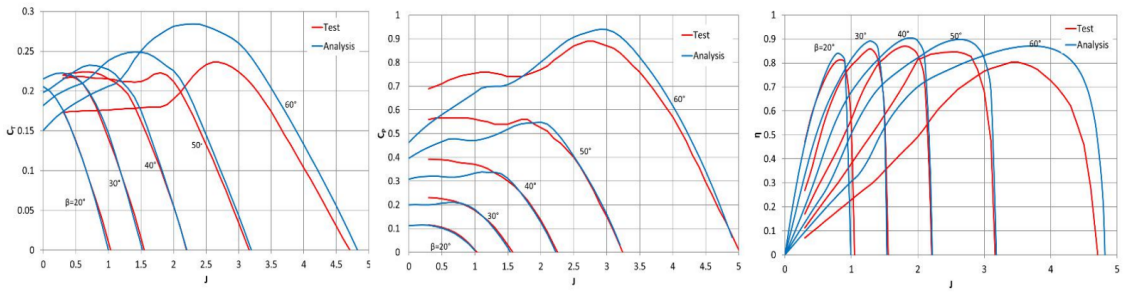

Figure 3.4. Change of propeller parameters for different values of pitch angle θ (in figure described as β). Reproduced from [19].

The largest thrust demands are expected to occur during the hover phase. Therefore the pitch angle should not be larger than approximately 20-30 degrees. The change of c_T for these angles is approximately linear with respect to the advance ratio J. The equation (3.10) shows that the advance ratio directly depends on v_{stream}. The resulting equations for thrust and torque can then be expressed as

$$F_T = (c_{T0} + c_T \cdot v_{stream}) \cdot \rho \cdot n^2 \cdot D^4, \tag{3.16}$$

$$Q_T = (c_{Q0} + c_Q \cdot v_{stream}) \cdot \rho \cdot n^2 \cdot D^5. \tag{3.17}$$

The equations can be further simplified by including the constants ρ and D in the parameters c. The final set of equations is

$$F_T = (c_{T0} + c_T \cdot v_{stream}) \cdot n^2, \tag{3.18}$$

$$Q_T = (c_{Q0} + c_Q \cdot v_{stream}) \cdot n^2. \tag{3.19}$$

The model assumes that v_{stream} is perpendicular to the propeller's rotational disk. In a non-zero radial wind speed $v_{\parallel}$ situation, the resulting thrust will be shifted from the center of rotation. This phenomenon is called *asymmetric blade effect*, and its effects are described in [20].

Such shift is difficult to measure and account for in the control algorithm accurately. However, it is relatively simple to limit its influence. The effect should be negligible, if the $v_{\parallel} \ll v_{tip}$. This requirement can be quantified by the relation

$$n_{\parallel} = \frac{v_{tip}}{v_{\parallel}}. \tag{3.20}$$

The number $n_{\parallel}$ determines how significant is the asymmetric distribution of thrust around the propeller. If $n_{\parallel} > 1$, the direction of airflow with respect to the airfoil does not change during rotation and the entire disc should generate positive thrust.

The asymmetric blade effect is impossible to eliminate. However, its influence on the position of the thrust vector can be included in the robustness analysis. The maximal uncertainty of the thrust vector position for $n_{\parallel} > 1$ can be written as

$$\Delta L_y = \frac{d_r \cdot D}{2}, \tag{3.21}$$

where $d_r = 1$ for the clockwise and -1 for the counter-clockwise rotating propellers. The variables for individual engines will be described by the upper index p, i, according to Figure 3.1.

3.4.2 Engine

The motor converts electric power, generated by the input voltage and current, to mechanical power. It is represented by torque and rotational velocity n of the propeller. The model assumes that the engine has its control unit, capable of providing the requested rotational speed n of the propeller. The resulting dynamics can be simplified into the first-order system with rise time τ [s].

$$\dot{n} = \frac{-n + n_{req}}{\tau} \tag{3.22}$$

3.5 Suspension system

The plane is expected to use tricycle-type landing gear with one wheel in the front and two under the wings. The basic geometry is described in Figure 3.5. The suspension is symmetric with respect to the aircraft's y-axis. The two rear wheels are L_x^{wr} [m] behind CG and the front one L_x^{wf} [m] in front of it. Roll stability depends on the lateral distance L_y^{wr} [m] between the rear wheels and the CG. The distances are measured in the Earth coordinate system. The model assumes a rigid body system.

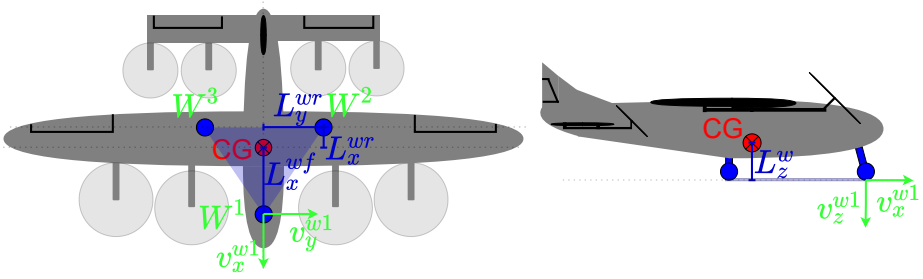

Figure 3.5. Basic suspension geometry. The light blue triangle represents the stability region for the CG position.

A sufficient description of generated forces can neglect the complex dynamics of the aircraft suspension. It can use simplified equations for generated forces, torques, and stability during landing.

The generated force can be approximated as the reaction force to the aircraft's relative down-force

$$F_z^{wi} = - F_{down}, \tag{3.23}$$

where F_{down} is a difference between the aircraft weight and overall lift force, acting on the wheels at the point of contact with the ground. Overall lift force includes thrust from the engines and aerodynamic surfaces.

The drag caused by the wheels is approximately

$$F_x^{wi} = - c_{roll} \cdot F_z^{wi}, \tag{3.24}$$

where $c_{roll} \in [0, 0.7]$ [21] is rolling friction coefficient. The described forces are only active when the relevant wheel is in contact with the ground.

The wheel's height is measured in the Earth coordinate system. It depends on the aircraft's roll and pitch angles. Therefore the suspension's static stability during landing depends on the airplane's attitude. An example of the stability region is in Figure 3.6.

If the aircraft roll and pitch combination is inside the depicted envelope, the suspension will create torque, pushing the aircraft to the horizontal attitude point. Outside the envelope, the torque will act in the opposite way and force the aircraft to roll over.

All the points at the triangle's perimeter that connects the suspension wheels are used to calculate the points on the maximal angle line. The vector from CG to each point is multiplied by $\arcsin(\frac{L_\perp}{L_z^w})$, where $L_\perp$ is the distance from CG to the point on the suspension triangle.

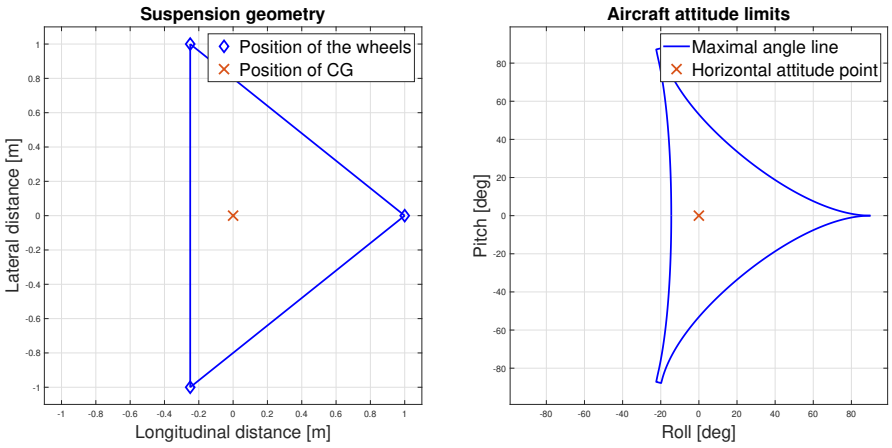

Figure 3.6. An example of attitude limits for stable landing and take off. The left figure depicts the position of wheels with respect to the mainframe CS. The right figure shows stability limits in the aircraft's attitude.

This description is not only useful for the suspension geometry design. It can also be considered during difficult landing scenarios. The attitude point with maximal distance from the angle line should ensure the largest stability margin.

3.6 Interaction between subsystems

So far, the individual subsystems have been defined independently. Each system interacts with the aircraft mainframe. Description of the relations can be done independently for each system, as shown in Figure 3.7. The figure depicts the linking variables between subsystems and the transformations of CS from the airframe to other subsystems and back.

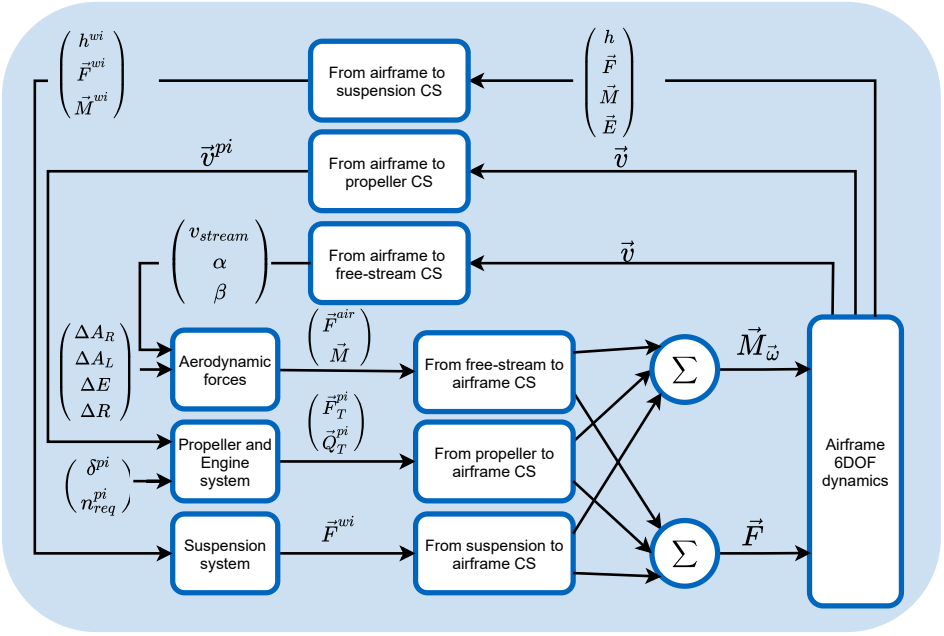

Figure 3.7. Schematic description of the interaction between individual systems

3.6.1 Free-stream system

This system is extensively utilized in section 3.3, where the lift and drag forces are described. These forces are defined in the free-stream CS. The transformation between the coordinate systems is defined by angles α and β, defined in equations (3.3) and (3.4). The airspeed in the free-stream CS is then expressed as rotation by α and β. Due to the nature of these angles, the rotation creates a velocity vector parallel to the free-stream x-axis. The value of this vector is v_{stream}.

The variables α, β, and v_{stream} are then used to calculate the forces in the free-stream CS. The rotation back to the airframe CS can be defined by the equation

$$\vec{F} = R_y(\alpha) \cdot R_z^T(\beta) \cdot \vec{F}^{air}, \tag{3.25}$$

where R_z is rotation matrix around z-axis and R_y around y-axis. The aerodynamic moments in equations (3.6) and (3.7) are already defined in the CS of the airframe and therefore no rotation transformation is needed.

3.6.2 Propeller and tilt engine systems

Each tilt engine CS is aligned with the mainframe CS. Therefore the transformation depends only on the engine position vector $L^{e,i}$. The transformation of velocities from mainframe to each tilt CS can be written as

$$\vec{v}^{e,i} = \vec{v} + \begin{pmatrix} 0 & L_z^{e,i} & -L_y^{e,i} \\ -L_z^{e,i} & 0 & L_x^{e,i} \\ L_y^{e,i} & -L_x^{e,i} & 0 \end{pmatrix} \vec{\omega}. \tag{3.26}$$

This definition is inspired by [16]. The transformation from tilt to propeller CS is done through rotation around y axis by tilt angle δ

$$\vec{v}^{p,i} = R_y(\delta^i) \cdot \vec{v}^{e,i}. \tag{3.27}$$

These definitions do not include the wind effect. The wind-speed vector can be added by rotating it from free-stream CS to the airframe CS and adding to the vector $\vec{v}$. The resulting vector $\vec{v}^{p,i}$ includes two values, used in section 3.4. The first is axial speed v_{stream}, that is equal to $\vec{v}_x^{p,i}$. The second is the radial speed, equal to $\vec{v}_z^{p,i}$. The velocity $\vec{v}_y^{p,i}$ is not considered, as it should be negligible in all the flight modes.

Together with specific propeller variables, these velocities are then used to calculate the thrust and torque of the propeller. Both vectors are aligned with the x-axis of the propeller's CS. The forces must be transformed back to the airframe CS. The transformation is linear and satisfies the definition of a generalized transformer [22]. This element uses the same modulus to transform generalized forces and flows, only in the opposite direction. Based on this, we can write the rotation of forces from propeller to tilt CS as

$$\begin{pmatrix} \vec{F}^{e,i} \\ \vec{M}^{e,i} \end{pmatrix} = (I_{2x2} \otimes R_y^T(\delta^i)) \cdot \begin{pmatrix} \vec{F}^{p,i} \\ \vec{M}^{p,i} \end{pmatrix}. \tag{3.28}$$

And the transformation from tilt to the airframe CS as

$$\vec{F} = F_{e,i} \tag{3.29}$$

$$\vec{M} = M_{e,i} + \begin{pmatrix} 0 & L_z^{e,i} & -L_y^{e,i} \\ -L_z^{e,i} & 0 & L_x^{e,i} \\ L_y^{e,i} & -L_x^{e,i} & 0 \end{pmatrix} \cdot F_{e,i}. \tag{3.30}$$

It should be noted that due to the nature of generated thrust and torque by the propeller, the vectors $\vec{F}^{e,i}$ and $\vec{M}^{e,i}$ should always have zero y-value. Therefore the relation (3.29) can be further simplified by removing the corresponding dependencies.

3.6.3 Suspension system

The suspension system generates forces based on the position of the wheels, determined by the aircraft's height and attitude. The relation can be written as

$$h^{wi} = h + R_{x,y}(\Phi, \Theta) \cdot \vec{L}^{wi}, \tag{3.31}$$

where is the height above the ground, $R_{x,y}$ is a matrix, that describes rotation around y and then x-axis, and $\vec{L}^{wi}$ is the wheels position vector. The relative downforce depends on the overall forces and moments acting on the aircraft. These values can be transformed into forces, aligned with the mainframe CS and centered at the suspension wheel with the equation

$$F_{wheel} = \vec{F} + (L_x^{wi})^{-1} \cdot M_y + (L_y^{wi})^{-1} \cdot M_x. \tag{3.32}$$

The force is then aligned with the Earth CS according to the aircraft's attitude.

$$F_{Down} = R_{x,y}(\Phi, \Theta) \cdot F_{wheel} \tag{3.33}$$

The reaction force (3.23) can then be transformed back to the aircraft CS by reversing the previously described transformation. Firstly, the force is aligned with the mainframe CS

$$F_{wheel}^{wi} = R_{x,y}^T(\Phi, \Theta) \cdot F_z^{wi}, \tag{3.34}$$

and then the force is transformed to CG according to the same fundamental relations, as for the tilt engine CS

$$\vec{F} = F^{wi}_{wheel}, \tag{3.35}$$

$$\vec{M} = \begin{pmatrix} 0 & L^{e,i}_z & -L^{e,i}_y \\ -L^{e,i}_z & 0 & L^{e,i}_x \\ L^{e,i}_y & -L^{e,i}_x & 0 \end{pmatrix} \cdot F^{wi}_{wheel}. \tag{3.36}$$

3.7 General aircraft dynamics description

The chapter has described complex VTOL aircraft dynamics for the entire flight envelope. Combining all previous relations should result in a sufficiently accurate plane model for control system design and analysis. These relations can be described as a general non-linear dynamical system

$$\frac{d\vec{x}}{dt} = f(x(t)) + g(x(t), u(t)), \tag{3.37}$$

$$y = h(x(t), u(t)), \tag{3.38}$$

where $\vec{x} = (\ \vec{L} \quad \vec{E} \quad \vec{v} \quad \vec{\omega}\ )^T$, $f(x)$ is autonomous part and $g(x, u)$ is controllable part of the system. The function $h(x, u)$ describes the output sensors. These dynamics can then be linearized in specific situations into linear state-space description

$$\frac{d\vec{x}}{dt} = A \cdot \Delta x + B \cdot \Delta u, \tag{3.39}$$

$$y = C \cdot \Delta x + D \cdot \Delta u, \tag{3.40}$$

where $A = \frac{\partial f(x)+g(x,u)}{\partial x}(x_0, u_0)$, $B = \frac{\partial g(x(t),u(t))}{\partial u}(x_0, u_0)$, $C = \frac{\partial h(x,u)}{\partial (x)}(x_0, u_0)$, $D = \frac{\partial h(x,u)}{\partial (u)}(x_0, u_0)$, $\Delta x = x - x_0$ and $\Delta u = u - u_0$.

However, this description can be unnecessarily complex. We can simplify these dynamics if we consider only specific flight conditions. These simplifications can reduce the complexity of a control system design and allow for a much simpler estimation of the model parameters to correspond with measured flight data.

In all the presented cases, the airframe dynamics are linearized as described in section 3.2.

3.8 Cruise mode dynamics

The first considered dynamics describe the plane during the cruise, with propellers parallel to the mainframe x-axis. This phase of flight operates with widely known relations, used in the aerospace industry and academia. The control surfaces generate torque vector, used to regulate the system attitude, and the engines provide forward thrust.

The autonomous dynamics of the aircraft are a combination of equations (3.5) and (3.6), where angles of attack and sideslip are expressed according to (3.3) and (3.4).

The control dynamics depend on the deflection of the aerodynamics surfaces, as described in (3.7), and on the thrust of the engines, described in (3.18). The input variables will then be deflection angles and rotational velocities of the propellers.

The aircraft dynamics are divided into the longitudinal, $x_{long} = (\ v_x \quad v_z \quad \omega_y\ )^T$, and the lateral, $x_{lat} = (\ v_y \quad \omega_x \quad \omega_z\ )^T$ part. The Euler angles and the position vector must be expressed independently and included into these dynamics as external parameters.

3.8.1 Longitudinal dynamics

The autonomous longitudinal dynamics of the aircraft follow the description

$$f\begin{pmatrix} v_x \\ v_z \\ \omega_y \end{pmatrix} = -\begin{pmatrix} C_d \cdot c_l^2 & 0 & C_{d0} \\ 0 & C_l & C_{l0} \\ 0 & b \cdot C_l & C_{l0} \end{pmatrix} \cdot \begin{pmatrix} \alpha^2 \\ \alpha \\ 1 \end{pmatrix} + \begin{pmatrix} -\sin\Theta \cdot m \cdot g \\ \cos\Theta \cdot m \cdot g \\ 0 \end{pmatrix}, \quad (3.41)$$

where parameters $C_x = P_D \cdot A \cdot c_x$. The relevant control variables are propeller speed and elevator deflection $u_{long} = (\, n \quad \Delta E \,)^T$. The control dynamics can be described as

$$g(\begin{pmatrix} v_x \\ v_z \\ \omega_y \end{pmatrix}, \begin{pmatrix} n \\ \Delta E \end{pmatrix}) = \begin{pmatrix} (c_{T0} + c_T \cdot v_\infty) \cdot n^2 \\ 0 \\ P_d \cdot A \cdot b \cdot c_{pa} \cdot \Delta E \end{pmatrix}. \quad (3.42)$$

3.8.2 Lateral dynamics

The autonomous lateral dynamics of the aircraft follow the description

$$f\begin{pmatrix} v_y \\ \omega_x \\ \omega_z \end{pmatrix} = \begin{pmatrix} -C_s \\ C_r \\ C_y \end{pmatrix} \cdot \arcsin\frac{v_y}{v_\infty}. \quad (3.43)$$

The control variables are ailerons and rudder deflection $u_{lat} = (\, \Delta A_R \quad \Delta A_l \quad \Delta R \,)^T$. The dynamics can be described as

$$g(\begin{pmatrix} v_y \\ \omega_x \\ \omega_z \end{pmatrix}, \begin{pmatrix} \Delta A_R \\ \Delta A_L \\ \Delta R \end{pmatrix}) = \begin{pmatrix} 0 & 0 & 0 \\ c_{ra} & -c_{ra} & 0 \\ c_{ya} & -c_{ya} & c_{yr} \end{pmatrix} \begin{pmatrix} \Delta A_L \\ \Delta A_R \\ \Delta R \end{pmatrix}. \quad (3.44)$$

3.8.3 Position and attitude dynamics

The description of these dynamics requires both longitudinal and lateral states. The autonomous equation can be written as

$$f\begin{pmatrix} \vec{L} \\ \vec{E} \end{pmatrix} = (I_{2x2} \otimes R_{xyz}^T(\Phi, \Theta, \Psi)) \cdot \begin{pmatrix} \vec{v} \\ \vec{\omega} \end{pmatrix}, \quad (3.45)$$

where R_{xyz} is a rotational matrix, describing sequential rotation around z, y and x-axis.

3.9 Hover dynamics

In this phase of flight, the plane hovers above a point or moves slowly. The aerodynamic effect does not need to be considered. The propellers are approximately aligned with the mainframe z-axis. The system is controlled through differential thrust and tilt of the propellers, an example of which is shown in Figure 3.8.

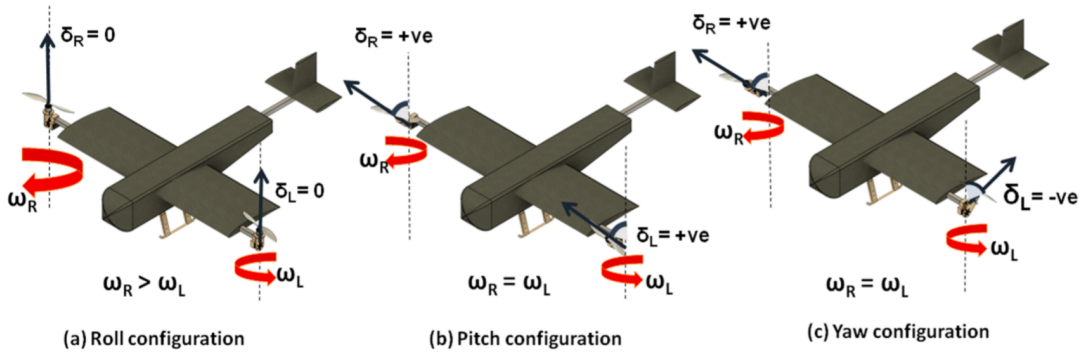

Figure 3.8. Example of hover control for two tilt propeller aircraft, where ω stands for rotor speed and δ for pitch angle. Reproduced from [23].

In hover, the aircraft's autonomous dynamics of rotation and translation velocities are approximately zero. The control dynamics are defined by the propeller's rotation speed and tilt angles. The dynamics also depend on the current engine torque, spinning the propellers. This effect could be neglected in cruise, as the propellers cancel each other out, but it is crucial in hover, typically for yaw control.

$$g(\begin{pmatrix} v_x \\ v_y \\ v_z \\ \omega_x \\ \omega_y \\ \omega_z \end{pmatrix}, \begin{pmatrix} n \\ \delta \end{pmatrix}) = \sum_{i=1}^{k} \begin{pmatrix} 1 & 0 & 0 & 0 \\ 0 & 0 & 0 & 0 \\ 0 & -1 & 0 & 0 \\ 0 & -L_y^{pi} & 0 & -d_r^i \\ L_z^{pi} & L_x^{pi} & 0 & 0 \\ -L_y^{pi} & 0 & -d_r^i & 0 \end{pmatrix} \cdot \begin{pmatrix} C_{T0}^i \cos\delta^i \cdot (n^i)^2 \\ C_{T0}^i \sin\delta^i \cdot (n^i)^2 \\ C_{Q0}^i \cos\delta^i \cdot (n^i)^2 \\ C_{Q0}^i \sin\delta^i \cdot (n^i)^2 \end{pmatrix} \quad (3.46)$$

It should be noted that the aircraft does not have direct control over its lateral velocity. Any outside disturbance can be compensated by changing the vehicle's attitude. The transformation between vehicle states and its attitude is described in section 3.8.3. If the disturbance is fixed to the aircraft frame, the system is unable to compensate for it.

The tilt-rotor dynamics in hover are similar to the mathematical description of drones, as derived in [24]. The main difference is the tilt-rotor's ability to tilt the propellers, which increases the number of actuation inputs. The ability to tilt propellers allows for decoupled the v_x and Θ control. The tilt angle can also be used for rotational velocity regulation, which is shown in [15].

3.10 Transition dynamics

During the transition from hover to cruise, the aircraft has an insufficient lift to keep itself in the air and must use the propeller's thrust to compensate for it. The model must therefore combine both cruise (section 3.8) and hover (section 3.9) dynamics. The autonomous equations are the same as in section 3.8.

The control equations are the combination of (3.42), (3.44) and (3.46). However, the thrust equations are more complicated in the transition mode than in previous cases, as the angle between propeller thrust and airspeed vectors is typically large. The resulting relations must include these angles in the thrust and torque equations.

$$F_T^i = (c_{T0}^i + c_T^i \cdot v_\infty \cos(\delta^i + \alpha)) \cdot (n^i)^2, \quad (3.47)$$

$$Q_T^i = (c_{Q0}^i + c_Q^i \cdot v_\infty \cos(\delta^i + \alpha)) \cdot (n^i)^2. \quad (3.48)$$

With this modification, the transition dynamics are complete.

3.11 Phases of flight

With all the primary modes of flight described, dividing the aircraft envelope into the described phases is necessary. As the dividing aspect, we will use the so-called load factor

$$\eta = \frac{L}{W}, \quad (3.49)$$

where L stands for the vertical force and W is the plane's weight. For horizontal flight, the η must be one. In the case of tilt-rotor VTOL, the load factors of the airframe and

propellers can be expressed independently. The overall η is then the sum of $\eta_{propellers}$ and $\eta_{airframe}$.

The hover phase expects negligible influence of aerodynamics. We can express this requirement in the form of maximal available load factor as $\eta^{max}_{airframe}(v_\infty) < 0.1$. This value corresponds to approximately 30 percent of stall speed (where the maximal wing load factor equals one).

Conventional aircraft are permitted to take off when their airspeed reaches 1.2 times the stall speed. For lower speeds, the plane is unable to maneuver safely. The minimal airspeed requirement can be expressed in load factor terms as $\eta^{max}_{airframe}(v_\infty) > 1.44$. This value can be used to start a cruise phase for VTOL aircraft.

The region where load factors are $0.1 < \eta^{max}_{airframe}(v_\infty) < 1.44$ is considered to be the transition phase. The entire flight envelope is shown in Figure 3.9, including the load factors and safe tilt angle regions.

The system expects a certain thrust-to-weight ratio of the propellers. This value must be greater than one and, for this example, was set to $\frac{T_{max}}{W} = 1.6$. Stall speed was set to 150 $[km \cdot h^{-1}]$ and lift to drag ratio $\frac{C_L}{C_D} = 2.5$. These values directly determine the division into the three phases of flight. Next, the drag of the aircraft must be compensated by the propellers. We can calculate minimal tilt angle for steady horizontal flight as

$$\delta_{min}(v) = \arccos\left(\frac{W \cdot C_D \cdot}{T \cdot C_L} \cdot \left(\frac{v}{v_{stall}}\right)^2\right) \tag{3.50}$$

and maximal tilt angle capable of horizontal flight as

$$\delta_{max}(v) = \arcsin\left(\frac{W \cdot \left(1 - \left(\frac{v}{v_{stall}}\right)^2\right)}{T_{max}}\right). \tag{3.51}$$

It should be noted that this simplification considers all used parameters as independent of flight speed and, therefore, can only be used for illustration of the expected V-η flight envelope.

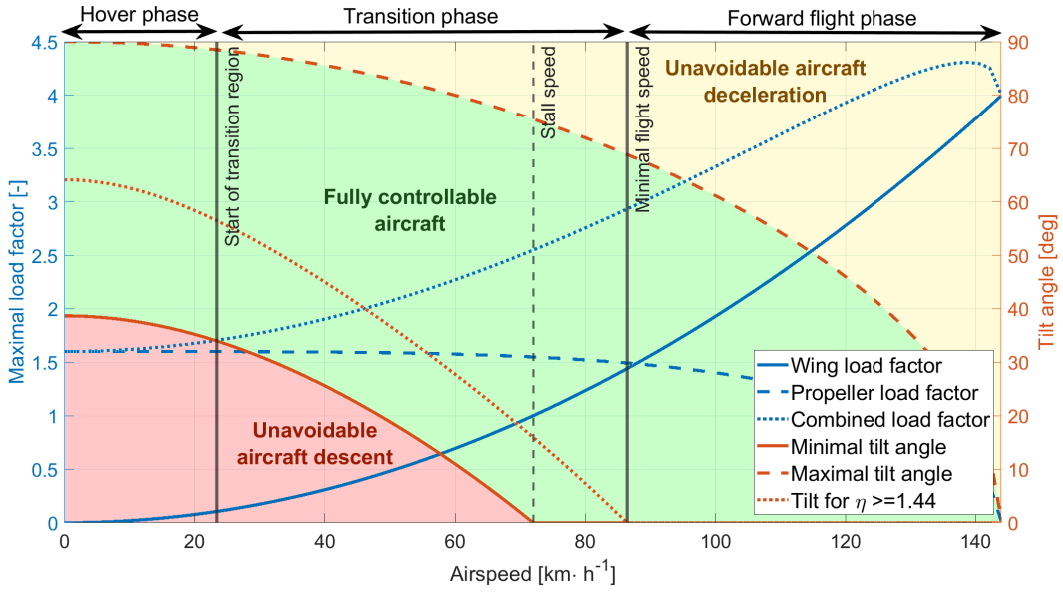

Figure 3.9. V-η Flight envelope for tilt-rotor VTOL aircraft. The blue lines represent load factors, and the red ones tilt angles. The tilt angle configuration region, capable of horizontal flight with constant speed, is colored green.

3.12 Summary

This chapter introduced a comprehensive description of aircraft flight dynamics. Individual parts of the system, mainly the airframe aerodynamics, the propellers, engines and suspension dynamics were discussed. Finally, the subsystems were combined through the transformation of coordinate systems. This complicated model was divided into three phases of flight to simplify the analysis and the control system design. The chapter ends with the introduction of the expected V-η flight envelope, based on load factors of propellers and aerodynamics of the airframe.

Chapter 4
Control law for aircraft regime

Designing a completely new control system for VTOL aircraft can be overwhelming for the designer and complicated to understand for the pilot. The importance of making the system intuitive for nowadays pilots should not be underestimated, as at least the first generations of VTOLs should be flown by human pilots.

A better approach would base the design on systems, common in the aerospace industry, and modify them for VTOL-capable aircraft. The general architecture can then be derived directly from current fly-by-wire systems and modified for VTOL-specific conditions.

In this chapter, the baseline aircraft architecture is introduced, together with the design of individual subsystems for the cruise.

4.1 Overall architecture

The control architecture, heavily inspired by [25], is shown in Figure 4.1. The cascade systems design allows for a simpler design, setup, and verification of individual subsystems. Each subsystem can be switched off to allow the pilot to take manual control over the controlled aircraft state and simplify the verification process.

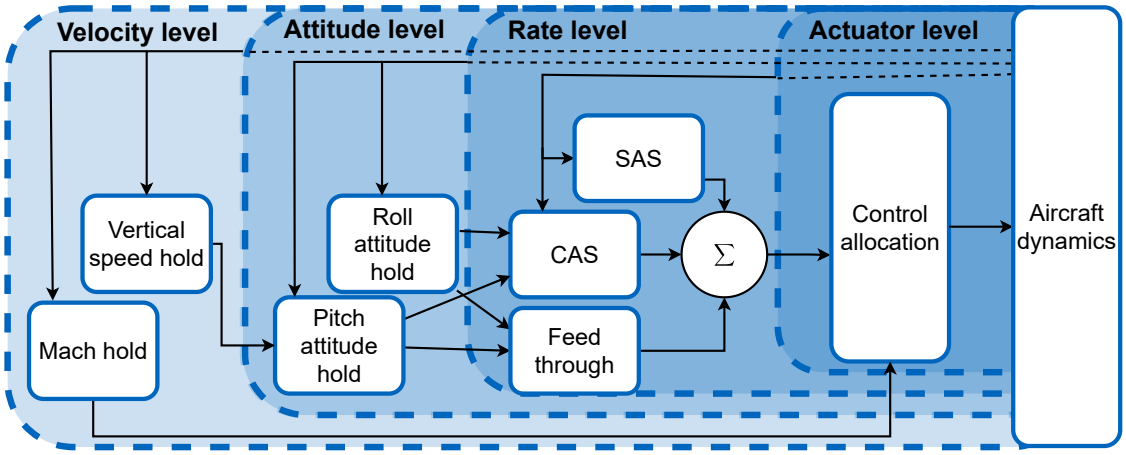

Figure 4.1. A description of general architecture design, depicting dependencies between control levels and subsystems.

The rest of the chapter describes individual subsystems in detail, beginning with the actuator level and continuing into greater abstract to the final velocity level system. Each section will start with a generic description of controlled aircraft dynamics, described in section 3.8, together with the system inputs and outputs. This baseline will then be used to propose specific controller subsystems and analyze the modified system stability with respect to the controller parameters.

4.2 Actuator level

This level aims to improve the aircraft controllability by allowing the higher-level system to request action of the actuators in the form of torques and forces requirements. The level calculates the desired actuator state so that the created torques and forces reflect the required ones.

The inputs into actuator level are torque vector $\vec{M}$, together with the average thrust force F_T. The propeller's tilt is assumed to be zero degrees. In a cruise, the controllable aerodynamic surfaces generate a moment on the plane, penalized by a slight drag increase. The engines mainly provide forward thrust but can also be used to create M_z torque using thrust vectoring. The outputs of this level are the requirements for deflection angles of the aerodynamic surfaces, as described in section 3.3.1 and propellers rotation speed, described in 3.4.1.

4.2.1 Aerodynamic surfaces control

The equation (3.7) describes the relationship between the deflection of aerodynamic surfaces and the moment acting on the airframe. It can be simplified by restricting $\Delta A_R = -\Delta A_L = \frac{\Delta A}{2}$. This assumption allows decoupling the deflection of the ailerons from M_y and M_z. The modified relation can be written as

$$\vec{M}\left(\begin{pmatrix} A \\ E \\ R \end{pmatrix}, v_\infty\right) = \begin{pmatrix} C_{ra}(v_\infty) & 0 & 0 \\ 0 & C_{pe}(v_\infty) & 0 \\ 0 & 0 & C_{yr}(v_\infty) \end{pmatrix} \cdot \begin{pmatrix} \Delta A \\ \Delta E \\ \Delta R \end{pmatrix} = C_{air} \cdot \begin{pmatrix} \Delta A \\ \Delta E \\ \Delta R \end{pmatrix} \quad (4.1)$$

where $C_{ij} = \frac{\rho \cdot v_\infty^2 \cdot A \cdot b}{2} \cdot c_{ij}$. The reversed relation can be obtained through matrix inversion, which is simple for diagonal matrices. The relation, describing how to deflect the aerodynamic surfaces according to the torque command, can be written as

$$\begin{pmatrix} \Delta A \\ \Delta E \\ \Delta R \end{pmatrix} = \begin{pmatrix} C_{ra}^{-1}(v_\infty) & 0 & 0 \\ 0 & C_{pe}^{-1}(v_\infty) & 0 \\ 0 & 0 & C_{yr}^{-1}(v_\infty) \end{pmatrix} \begin{pmatrix} \Delta M_x \\ \Delta M_y \\ \Delta M_z \end{pmatrix}. \quad (4.2)$$

This function has singularity at $v_\infty = 0$. This issue can be solved with restricting the airspeed into region $\{v_\infty \in R | v_\infty > 0\}$. We can also limit the usage of aerodynamic surfaces below a certain minimum speed to prevent rapid and unnecessary oscillations due to insufficient control authority.

Another issue is that system depends on the aircraft's airspeed. This value is typically measured with a pitot tube, but the measurements can be rather noisy. The noise can be created from different sources, but it can be generalized as additive noise $e \approx N(0, R)$. The measured value of airspeed v_∞^m can be written as

$$v_\infty^m = v_\infty + e. \quad (4.3)$$

The gain in equation (4.2) depends on $\frac{1}{v_\infty^2}$. The question now is: What kind of multiplicative error should we expect if we use the value v_∞^m instead of v_∞. The error can be expressed as

$$E = \frac{(v_\infty^m)^2}{v_\infty^2} = \frac{v_\infty^2 + 2 \cdot e \cdot v_\infty + e^2}{v_\infty^2} \approx N\left(\frac{v_\infty^2 + R}{v_\infty^2}, \frac{2 \cdot R \cdot (2 \cdot v_\infty^2 + R)}{v_\infty^4}\right), \quad (4.4)$$

where R is noise variance. The error has a mean value shifted by R. We can eliminate this issue by subtracting the noise variance from the calculated airspeed squared.

Lastly, we can see that the error variance decreases with increasing airspeed. We can find the $v_{\infty,min}$ and R combination, where the error will be smaller than the predefined value E_{max} with n_σ degree of confidence with the usage of the equation

$$E_{max} - 1 = n_\sigma \cdot \sqrt{\frac{2 \cdot R \cdot (2 \cdot v_\infty^2 + R)}{v_\infty^4}} \quad , (4.5)$$

where $n_\sigma = 1, 2, 3$ corresponds to 68, 95 and 99 percent confidence levels. The value E_{max} has a direct influence on the performance of all higher-level control systems. At speeds below v_∞^{min} the system robustness can not be ensured. The gain scheduling should be replaced with a fixed matrix in these conditions. The last issue is that the current v_∞ is not known. To ensure that the aircraft is operating with sufficient airspeed, the measured values should be greater than $v_\infty^{min} + n_\sigma \cdot \sqrt{R}$.

4.2.2 Propeller speed control

The relation between propeller rotational speed and the generated thrust is described in equation (3.18). From this equation, the required propeller speed can be expressed as

$$n = \sqrt{\frac{F_T^{req}}{c_{T0} + c_T \cdot v_\infty}} \quad (4.6)$$

The mean value of coefficients can be used to calculate the average rotational speed for all propellers. Another option would be determining the optimal thrust distribution between individual engines and calculating each propeller's speed individually.

The engines also generate torque around the z and y-axis of the aircraft. The pitch torque depends on the vertical position of the engines. It typically can not be used for control, as all engines are either above or below the CG. Therefore this value is only considered a disturbance that needs to be compensated. The value of pitch torque generated by propellers can be expressed as

$$M_y = L_z \cdot (c_{T0} + c_T \cdot v_\infty) \cdot n^2 \quad (4.7)$$

The yaw torque generated by the propellers is much more interesting. Electric engines typically have a significantly faster response time when compared to combustion engines. This allows for the direct use of thrust vectoring for yaw control, similar to lateral stabilization systems in modern vehicles. The torque can be expressed as

$$M_z = -L_y \cdot (c_{T0} + c_T \cdot v_\infty) \cdot n^2 \quad (4.8)$$

This non-linear relation can be linearized at the average propeller speed, calculated from F_T^{req}. The derivation with respect to n^i is

$$\frac{\partial M_z}{\partial n^i}(n^i) = -2 \cdot L_y \cdot (c_{T0} + c_T \cdot v_\infty) \cdot n^i = c_{M_{z,n}}(v_\infty, n^i) \cdot \partial n^i. \quad (4.9)$$

For the entire vector $\vec{n}$ it can be expressed as

$$\frac{\partial M_z}{\partial \vec{n}}(\vec{n}) = \vec{c}_{M_{z,n}}(v_\infty, \vec{n}) \cdot \partial \vec{n} \quad (4.10)$$

The exact inverse of this relation can not be exactly calculated, as $\vec{c}_{M_{z,n}}(v_\infty, \vec{n}) = \vec{c}_{M_{z,n}}$ is a row vector. However, a pseudo-inversion method can be used to get the required results.

$$\partial\vec{n} = \vec{c}^{T}_{M_{z,n}} \cdot (\vec{c}_{M_{z,n}} \cdot \vec{c}^{T}_{M_{z,n}})^{-1} \frac{\partial M_z^{req}}{\partial \vec{n}} \tag{4.11}$$

The M_z^{req} can be achieved with rudder deflection but also with thrust vectoring of the propellers. This over-actuation can be solved using complex optimization or some form of heuristic approach. For example, preferring the usage of rudder and only using the thrust vectoring when the rudder authority is insufficient.

The aerodynamic surfaces and propeller speed control allow tracking of the desired torques and forces acting on the aircraft.

4.3 Rate level

This level aims to modify and unify the aircraft rotational velocities dynamics. Typically, the rate level systems improve the aircraft handling by modifying short period modes. This is done through two feedback laws, called stability and control augmentation systems (SAS and CAS). These designs complement the pilot commands, so a feed-forward system should be implemented as well.

The inputs for this level are the aircraft rotational rates, measured by a gyroscope or similar system, and the pilot's input. Outputs are torque commands for the previous level.

4.3.1 Stability augmentation system (SAS)

The purpose of SAS is to increase aircraft stability through filtered feedback from the measured rotational rates. The system seemingly increases the aircraft's resistance to fast changes of attitude, increasing the aircraft's stability. The control scheme is depicted in Figure 4.2.

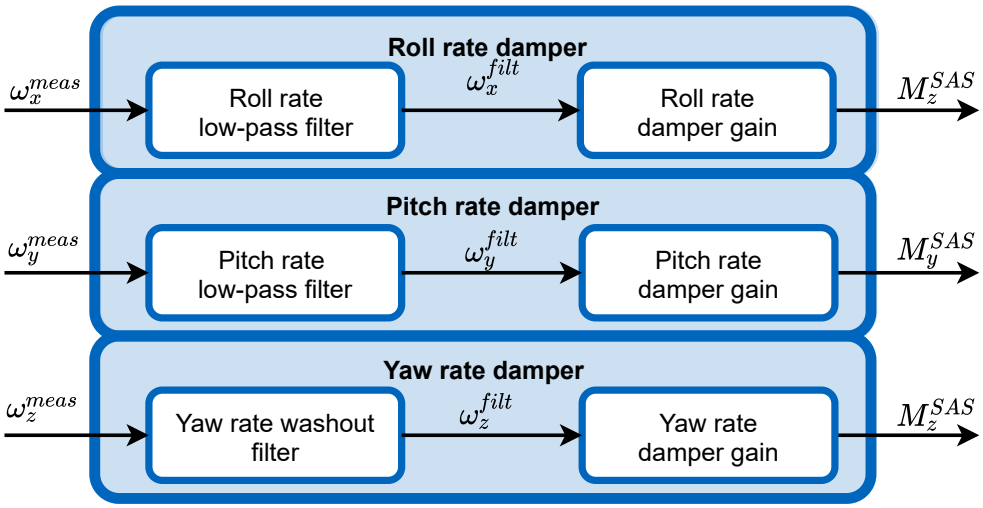

Figure 4.2. A description of the stability augmentation system design scheme.

Individual systems can be designed through division into longitudinal and lateral dynamics, as described in section 3.8.

The considered longitudinal dynamics are only the short period modes. The phugoid mode is mostly unaffected [25, p.288]. The SAS system uses filtered pitch rate to increase the damping of these modes. In some instances, the system also uses α-feedback if the aircraft stability is insufficient. This loop is not considered as the SAS system would then depend on another sensor. The α dynamics will be resolved in a higher-level system.

The lateral dynamics mainly deal with the so-called dutch roll mode. This roll and yaw movements combination is reduced through a yaw rate damper. The yaw rate should not be entirely dampened, as any turn maneuver creates a desired non-zero value. A washout filter can prevent an unwanted dampening of slow changes in yaw due to turns, as described in [25, p.295]. The roll rate damper is typically only used to reduce the changes in the aircraft behavior with changing airspeed.

4.3.2 Feed-forward gain

The damped system response with damper gain G_D, pilot feed-forward gain G_{FF}, and actuator rise time τ can be modeled as a second-order system, assuming that the damper influence is much larger than the airframe drag. The transfer function for any rotational velocity is then

$$tf(s) = \frac{G_{FF} \cdot \tau^{-1}}{s^2 + \tau^{-1} \cdot s + G_D \cdot \tau^{-1}}, \tag{4.12}$$

with DC gain $\frac{G_{FF}}{G_D}$. The feed-forward gain can be used to set the DC gain as desired.

4.3.3 Control augmentation system (CAS)

The SAS design is a Type 0 controller. This means that it is unable to keep zero steady-state error. This property is desired as the system does not use inputs from the pilot. However, it also means that the SAS system will not suppress any differences between the actual plane and the mathematical model. A CAS architecture can be implemented to provide more accurate tracking of the pilot command. The system compares measured aircraft responses with a mathematical model and regulates the difference. For this purpose, a Type 1 regulator (typically PI) is used. A general architecture is shown in Figure 4.3.

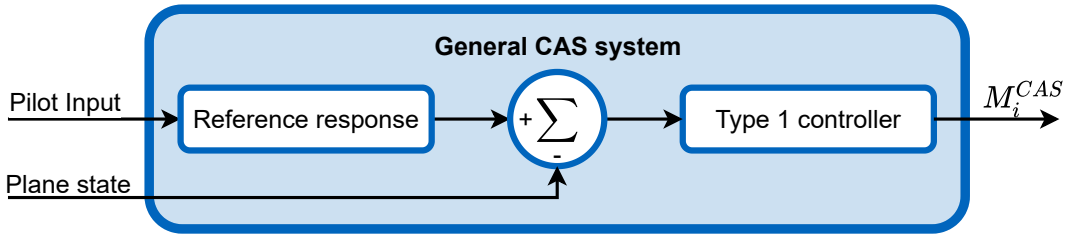

Figure 4.3. A description of control augmentation system design scheme.

The reference model can be used in the form of the transfer function (4.12), ideally fitted to the aircraft behavior. It should be noted that the yaw dynamics must include the yaw rate caused by a steady-state turn. Its value can be estimated by modifying equation [25, 4.6-4] with approximating pitch angle $\Theta \approx 0$ into the form

$$\omega_z(\Phi, v_\infty) = \frac{g \cdot \tan(\Phi)}{v_\infty}, \tag{4.13}$$

where Φ is roll angle and g is the gravitational acceleration. As the system only regulates the deviation from the model, the controller can have a much more aggressive response than in the case of direct rotational rates control architecture, typically used in drone applications.

4.4 Attitude level

The rate control systems can simplify most aircraft dynamics into easily controllable machines. However, the pilot is still required to regulate the aircraft's attitude state through continuous commands. Attitude control systems, called roll and pitch hold, were introduced to limit pilot fatigue. These systems are typically intended to reduce the pilot's workload by keeping the current aircraft's attitude.

The controlled variables are pitch and roll angles, regulated through commands for rotational rates, sent to lower-level systems. The controlled system is assumed to be the serial connection of dynamics (4.12) and an integrator, with external disturbances caused by aerodynamic effects, described in section 3.3.

The design typically uses PI or a similar Type 1 controller, combined feed-forward control, and model reference response. The general description is shown in Figure 4.4.

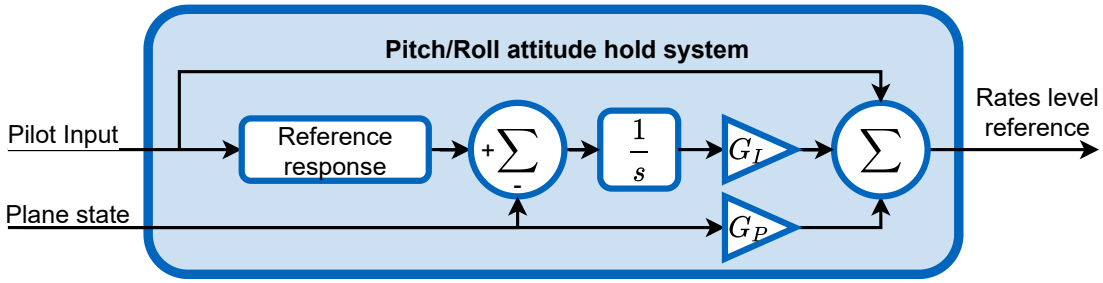

Figure 4.4. A description of the general attitude hold system scheme.

The gain G_p, represents the feedback part of the typical P regulator. As described in section 4.3, these pure feedback gains, independent of pilot input, are used to increase the aircraft stability around zero state value. The resulting combination of system dynamics and feedback damper G_p results in third-order dynamics

$$tf(s) = \frac{G_{FF} \cdot \tau^{-1}}{s^3 + \tau^{-1} \cdot s^2 + G_D \cdot \tau^{-1} s + G_{FF} \cdot G_p \cdot \tau^{-1}}, \tag{4.14}$$

These dynamics do not allow for an independent setup of steady-state gain and pole placement. This issue can be solved through the introduction of additional feed-forward gain.

The introduced dynamics do not consider the influence of aerodynamic forces created by the angle of attack and sideslip angle of the airframe. Full dynamics are due to these effects more complicated, as shown in examples from [25, p. 322-329].

The influence of aerodynamics forces on the attitude dynamics can be mitigated by using a feedback integrator with gain G_I. The component can compensate for these effects, which is especially useful when aerodynamic variables are not measured, or the provided model is not accurate enough. This requires a robust design approach to ensure stable behavior during the entire flight envelope.

The influence of aerodynamics forces depends on the squared value of the aircraft's airspeed. If the flight envelope is significant, a single configuration does not have to be sufficient. The solution to this problem can be a pre-computed gain scheduling system, dependent on the aircraft's airspeed.

4.5 Velocity level

The previous control levels have dealt with the attitude dynamics. However, the pilot still controls the aircraft's longitudinal velocity and altitude. Autopilots responsible for controlling these plane states are so-called Altitude and Mach hold systems. For the purpose of this thesis, the altitude hold is replaced with a Climb rate (V_z) hold system.

4.5.1 Climb rate hold system

The goal of the V_z hold controller is to track the desired aircraft vertical velocity. A control over force F_z must be enabled to achieve the tracking. As described in equation (3.5), the aerodynamic force F_z^{air} depends on the angle of attack α. In horizontal flight, this force is dominant and must compensate for the pull of gravity. The case of climb and descend is slightly different, as the force from the engines starts to have a significant role as well. Only horizontal flight mode is considered for the architecture design, as shown in Figure 4.5.

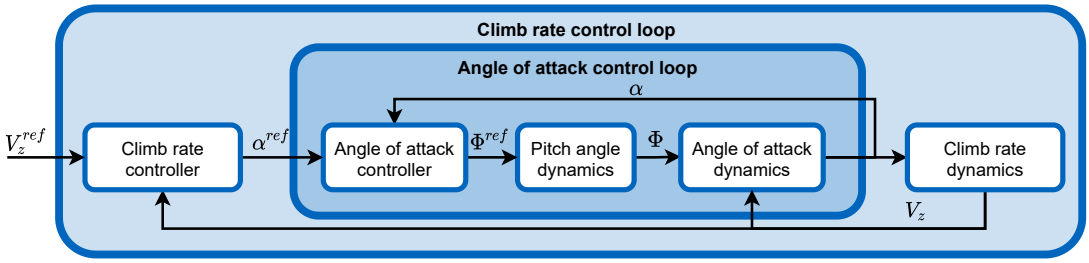

Figure 4.5. A basic description of Climb rate hold system.

The V_z hold system uses the angle of attack to generate the desired vertical force. This means that an additional system, controlling the angle of attack, must also be implemented. The issue with the α control is that the dynamics have derivative nature, similar to the angle of sideslip in vehicles, as described in [26]. This nature requires a Type 1 regulator for α controller. Still, the resulting system's step response has a non-zero steady-state error. The considered pitch angle dynamics include the pitch attitude hold system described in the previous section.

As described in [25, p.330], the attitude or V_z hold systems should mainly affect the phugoid modes, with negligible influence on short period modes of the aircraft. Due to this fact, these higher-level systems can have a much slower response time than the previous levels.

4.5.2 Mach hold system

The Mach hold controller tracks the desired plane airspeed v_∞ through thrust command F_T^{req}, which is then transformed into propeller speed at the actuator level according to equation (4.6). The controlled dynamics depend on aerodynamic drag and gravity force acting perpendicular to the lift vector. In horizontal level flight, the influence of gravity can be neglected. The transfer from required thrust to airspeed can be written as a first-order system with a time constant and gain $\frac{1}{C_D(\alpha, v_\infty)}$, where $C_D(\alpha, v_\infty)$ represents aerodynamic drag, linearized at given airspeed and angle of attack. A simple PI controller is sufficient to control these dynamics.

4.6 Summary

This chapter describes aircraft control systems commonly used in the aerospace industry. These architectures are familiar to most pilots and are a great starting point for designing a fly-by-wire system for VTOL aircraft. The typical implementation of these systems uses linearized aircraft models, which is challenging for the entire flight envelope of a VTOL plane. For this reason, the systems were modified to allow for a simpler implementation of these capabilities.

Chapter 5
VTOL capable fly-by-wire system

This chapter focuses on modifying control laws, introduced in the previous chapter, to allow for flight operations from stall speed to vertical hover. Also, the design goal is to allow for a seamless transition from hover phase to cruise mode. This means that general architecture remains the same as in Figure 4.1. The chapter describes modifications of individual subsystems from the previous chapter in the same order.

5.1 Actuator level

The main difference from cruise mode is that the engines can change their tilt angle. The modification enables complete torque control through changes in the propeller's speed and tilt angle. This ability is crucial during low-speed maneuvers, as the authority of control surfaces is insufficient.

The first step in expanding the capabilities of thrust vectoring is to describe the forces generated by the engines. This has been done in section 3.6, where the transformation equations (3.28) and (3.29) describe the influence of a single engine's force on the moment vector around the aircraft CG. These equations can be expanded into the following form

$$\vec{M}^i = \begin{pmatrix} -L_y^{e,i} \cdot \sin(\delta^i) & \cos(\delta^i) \cdot D^i \\ L_x^{e,i} \cdot \sin(\delta^i) + L_z^{e,i} \cdot \cos(\delta^i) & 0 \\ -L_y^{e,i} \cdot \cos(\delta^i) & -\sin(\delta^i) \cdot D^i \end{pmatrix} \begin{pmatrix} (c_{T0} + c_T \cdot v) \cdot (n^i)^2 \\ (c_{Q0} + c_Q \cdot v) \cdot (n^i)^2 \end{pmatrix} \quad (5.1)$$

where $v = v_{stream}$. By differentiating the equation (5.1) by δ^i and n^i, we will get the linearized form of this function, localized at the current tilt angle, airspeed, and average propeller rotational speed, received from the pilot. If we assume that only time-dependent variables are the tilt angle and rotational speed, we can express the derivation with respect to time as

$$\frac{d\vec{M}^i}{(dt)}(\delta_0^i, n_0^i) = \frac{\partial \vec{M}^i}{\partial \delta^i}(\delta_0^i, n_0^i) d\delta^i + \frac{\partial \vec{M}^i}{\partial n^i}(\delta_0^i, n_0^i) dn^i, \quad (5.2)$$

where

$$\frac{\partial \vec{M}^i}{\partial \delta^i}(\delta_0^i, n_0^i) = \begin{pmatrix} \left(-L_y^{e,i} \cos(\delta_0^i) \cdot C_T - D^i \cdot \sin(\delta_0^i) \cdot C_Q\right) \cdot (n_0^i)^2 \\ (L_x^{e,i} \cos(\delta_0^i) - L_z^{e,i} \sin(\delta_0^i)) \cdot C_T \cdot (n_0^i)^2 \\ (L_y^{e,i} \cdot \sin(\delta_0^i) \cdot C_T - D^i \cdot \cos(\delta_0^i) \cdot C_Q) \cdot (n_0^i)^2 \end{pmatrix} \quad (5.3)$$

$$\frac{\partial \vec{M}^i}{\partial n^i}(\delta_0^i, n_0^i) = \begin{pmatrix} 2 \cdot (-L_y^{e,i} \sin(\delta_0^i) \cdot C_T + D^i \cdot \cos(\delta_0^i) \cdot C_Q) \cdot (n_0^i) \\ 2 \cdot (L_x^{e,i} \sin(\delta_0^i) + L_z^{e,i} \cos(\delta_0^i)) \cdot C_T \cdot (n_0^i) \\ 2 \cdot (-L_y^{e,i} \cdot \cos(\delta_0^i) \cdot C_T - D^i \cdot \sin(\delta_0) \cdot C_Q) \cdot (n_0^i) \end{pmatrix}. \quad (5.4)$$

Furthermore, the derivation of overall torque vector $\vec{M} = \sum_i \vec{M}$ with respect to individual M_i results in a row vector of size $1 \times n_e$, where n_e is the number of engines. A chain rule can now be used to create $3 \times 2n_e$ matrix C, describing the total

derivative of $\vec{M}$ with respect to t. Lastly, column exchange can be used to reorder the matrix C into the form

$$\frac{d\vec{M}}{(\,dt\,)}(\vec{\delta}_0, \vec{n}_0) = C_{prop}(\vec{\delta}_0, \vec{n}_0) \begin{pmatrix} d\vec{\delta} \\ d\vec{n} \end{pmatrix}. \tag{5.5}$$

The next step is to inverse the relation to express the change of tilt and rotational speed according to the required change of torque. The matrix C_{prop} is not square, and therefore direct inverse can not be used. Instead, the same pseudo inversion used in propeller speed control, described in section 4.2, should be used. The resulting relation can be expressed as

$$\begin{pmatrix} d\vec{\delta}^{req} \\ d\vec{n}^{req} \end{pmatrix} = C^{+}_{prop}(\vec{\delta}_0, \vec{n}_0)\vec{M}^{req} = C^{T}_{prop} \cdot (C_{prop} \cdot C^{T}_{prop})^{-1} \cdot \vec{M}^{req}, \tag{5.6}$$

where $\vec{M}^{req} = \frac{d\vec{M}}{dt}(\vec{\delta}_0, \vec{n}_0)$. Issues with this approach depend on the inversion $(C \cdot C^T)^{-1}$. The first issue is to ensure that inversion exists. This can be checked through the determinant of $C \cdot C^T$, which can not be zero. Another complication is the computational intensity of matrix inversion. The $C \cdot C^T$ matrix has a size 3×3. Inversion of a matrix this size can be done through efficient algorithms and should not significantly affect the overall system's computational intensity. Also, the inversion needs to be calculated only when its inputs, namely mean tilt angle, the rotational speed of propellers, and aircraft velocity, change significantly. These dynamics are relatively slow, and therefore the update frequency for this matrix can be much slower than for the remaining control systems.

5.1.1 Inaccuracies and uncertainties of the calculations

Similar to the dynamic inversion for control surfaces, described in section 4.2.1, the accuracy of the above relations with respect to uncertain parameters should be described. Fortunately, these calculations are less sensitive to airspeed measurements, which are expected to be noisy. The only variables, depending on airspeed are $C_T = c_{T0} + c_T \cdot v_{stream}$ and $C_Q = c_{Q0} + c_Q \cdot v_{stream}$. These constants are reduced to half of their size at half of the maximal achievable speed. The other unknown dynamical variables are propeller speed and tilt angle, which are directly controlled, and their uncertainties can be expected to be negligible. Another source of error is unknown values of static parameters, such as distances of propellers from the engines. As the overall number of parameters is quite large, a Monte Carlo method can be used to calculate the overall inaccuracy of the calculations.

Another issue is linearization error. The method approximates the original function well for small deviations of $d\vec{\delta}$ and $d\vec{n}$.

The tilt angle $\vec{\delta}$ is only used as an argument for sin and cos functions, for which the linear approximations are typically considered accurate up to five degrees deviation. This limitation is simple to implement. However, it can reduce the aircraft's controllability in certain situations. If the issue is present, the saturation must be increased, but then the linearization error should not be neglected.

The propeller speed $\vec{n}$ is unfortunately used as an argument for a quadratic function. The method, especially for small $\vec{n}$, overshoots the accurate values of $d\vec{n}$ and results in larger torque than required. This issue is typically negligible for large values $\vec{n}$, where even small $d\vec{n}$ can generate large torque. In a simplified situation, where the torque is generated by one engine through a relation

$$M_{real} = c \cdot n^2, \tag{5.7}$$

the multiplicative error can be expressed as

$$E = \frac{c \cdot (n + dn)^2 - c \cdot n^2}{M_{corr}} = \frac{c \cdot (n + 0.5 \cdot c^{-1} n^{-1} \cdot M_{corr})^2 - c \cdot n^2}{M_{req}}, \tag{5.8}$$

from which the corrected torque request M_{corr} can be found by solving the equation for $E = 1$. The solution can be written as

$$M_{corr} = 2 \cdot n \cdot \sqrt{c} \cdot \sqrt{c \cdot n^2 + M_{req}} - 2 \cdot n^2 \cdot c. \tag{5.9}$$

The equation (5.8) can also be used to determine the minimum value of n_{min}, for which the multiplicative error is smaller than some threshold $E_{max} > 1$, assuming $M_{req} = M_{corr}$. The relation depends on maximal expected torque request M_{req}^{max} and can be expressed as

$$n_{min} = \sqrt{\frac{M_{req}^{max}}{4 \cdot c \cdot (E_{max} - 1)}} \tag{5.10}$$

This relation can also be expanded for multiple engines by approximating c with the mean of individual c^i, multiplied by the number of engines. The resulting n_{min} can be used to determine the range of n in which the control design can be considered valid. Bellow the n_{min}, system stability can be achieved by reducing the M_{req} linearly from $n = n_{min}$, where the gain is 1 to $n = 0$, where the gain is 0.

5.1.2 Combination of engines and aerodynamic surfaces

With sufficient authority both from propellers and aerodynamic surfaces, a combination of these actuators should be implemented. The simplest option would be to add matrix C_{air} from equation (4.1) to matrix C from equation (5.5) and re-calculate the pseudo-inversion. However, this approach can create undesired over-actuation of ineffective systems and does not increase robustness to physical limitations of actuators. A better approach is to use a sequential design, where one type of actuator is used first, and the second group solves the torque reminder created by the physical attributes of the system. Based on the provided hardware abilities, this approach can be expanded further to eliminate system error through non-linear estimation of created torque or using cyclic calculations to ensure minimum possible error. A basic description of the sequential design is shown in Figure 5.1.

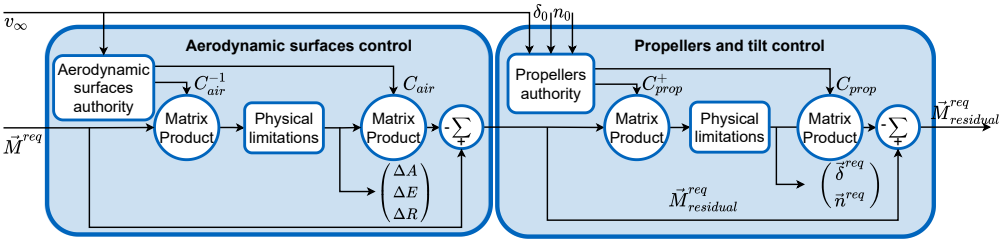

Figure 5.1. A basic implementation of the sequential actuators approach, based on equations (4.1), (4.2), (5.5) and (5.6).

5.2 Rate and Attitude levels

The main advantage of the design, proposed in Chapter 4, is that the rate level output uses torque command instead of direct control of aerodynamic surfaces. Due to this design feature, no modifications are needed for the VTOL system design. In fact, the transfer functions, describing both rates and angles level dynamics, are more accurate as the aerodynamic effects are less significant.

5.3 Velocity level

Unlike in Chapter 4, the thrust of the propellers can be used for both upward and forward forces generation. Also, the propeller's speed and tilt angle can completely change its influence on the generated forces during the flight. For example, during hover, propeller speed generates F_z force, while changing tilt influences F_x. In cruise, the roles are switched. This phenomenon complicates the controller design and prevents the usage of linear system architecture. Instead, an exact linearization method can compensate for the system's non-linearity and decouple the aircraft's vertical and forward speed dynamics.

First step is to describe the dynamics of the system in form $\dot{\vec{x}} = f(\vec{x}) + g(\vec{x}) \cdot \vec{u}$. This design is optimal for the exact linearization method. The systems state vector includes $v_x = x_1$, $v_z = x_2$, $\delta = x_3$ and $n = x_4$ variables. The control inputs are the derivatives of tilt angle $\dot{\delta}$ and propeller speed $\dot{n}$. The resulting dynamics have the form

$$\begin{pmatrix} \dot{x}_1 \\ \dot{x}_2 \\ \dot{x}_3 \\ \dot{x}_4 \end{pmatrix} = \begin{pmatrix} \frac{\cos x_3 \cdot (c_{T0} + c_T \cdot x_1) \cdot x_4^2 + F_x^{ext}}{m} \\ \frac{-\sin x_3 \cdot (c_{T0} + c_T \cdot x_1) \cdot x_4^2 + F_z^{ext}}{m} \\ 0 \\ 0 \end{pmatrix} + \begin{pmatrix} 0 & 0 \\ 0 & 0 \\ 1 & 0 \\ 0 & 1 \end{pmatrix} \cdot \vec{u}, \tag{5.11}$$

where F_x and F_z represent the external forces generated by aerodynamics or other not considered influences. The output vector $\vec{y}$ consists of $y_1 = x_1$ and $y_2 = x_2$. The next step is to derive the state vector $\vec{z}$, which will represent dynamics in the linear dimension. The procedure is described in [27]. As the method is commonly known, the individual steps and conditions are not discussed in detail. The resulting $\vec{z}$ can be expressed as

$$\begin{pmatrix} z_1 \\ z_2 \\ z_3 \\ z_4 \end{pmatrix} = \begin{pmatrix} y_1 \\ \dot{y}_1 \\ y_2 \\ \dot{y}_2 \end{pmatrix} = \begin{pmatrix} x_1 \\ \dot{x}_1 \\ x_2 \\ \dot{x}_2 \end{pmatrix} \tag{5.12}$$

The autonomous compensation vector $\vec{F}$, that ensures linearization of the dynamics without any control can be written as

$$\vec{F} = \begin{pmatrix} \nabla_x z_2(\vec{x}) \cdot f(\vec{x}) \\ \nabla_x z_4(\vec{x}) \cdot f(\vec{x}) \end{pmatrix} = \begin{pmatrix} \frac{c_T \cdot x_4^2 \cdot \cos(x_3) \cdot \dot{x}_1}{m} \\ -\frac{c_T \cdot x_4^2 \cdot \sin(x_3) \cdot \dot{x}_1}{m} \end{pmatrix} \tag{5.13}$$

The linear control vector $\vec{v}$ has the form

$$\vec{v} = \begin{pmatrix} \nabla_x z_2(\vec{x}) \cdot (f(\vec{x}) + g(\vec{x}) \cdot u) \\ \nabla_x z_4(\vec{x}) \cdot (f(\vec{x}) + g(\vec{x}) \cdot u) \end{pmatrix} = \vec{F} + \begin{pmatrix} \frac{\partial \dot{x}_1}{\partial x_4} \cdot u_2 + \frac{\partial \dot{x}_1}{\partial x_3} \cdot u_1 \\ \frac{\partial \dot{x}_2}{\partial x_4} \cdot u_2 + \frac{\partial \dot{x}_2}{\partial x_3} \cdot u_1 \end{pmatrix}. \tag{5.14}$$

The relation between $\vec{v}$ and the original input vector $\vec{u}$ can be expressed through matrix D as

$$\vec{v} = D \cdot \vec{u}, \tag{5.15}$$

where $D = \nabla_u \vec{v}$. However, the more useful matrix than D is its inverse D^{-1} as it can be used to derive real control inputs u from the linearized and virtual $\vec{v}$. This matrix has the following form

$$D^{-1} = \begin{pmatrix} \frac{-m \cdot \sin(x_3)}{(c_{T0} + c_T \cdot x_1) \cdot x_4^2} & \frac{-m \cdot \cos(x_3)}{(c_{T0} + c_T \cdot x_1) \cdot x_4^2} \\ \frac{-m \cdot \cos(x_3)}{2 \cdot (c_{T0} + c_T \cdot x_1) \cdot x_4} & \frac{-m \cdot \sin(x_3)}{2 \cdot (c_{T0} + c_T \cdot x_1) \cdot x_4} \end{pmatrix}. \tag{5.16}$$

The inversion does not exist for zero propeller speed $x_4 = 0$. This complication can be solved by requiring some minimal propeller speed $x_4^{min} > 0$. The requirement should be implemented as saturation of the x_4 state before entering the exact linearization algorithm so that the system still works even with stopped propellers. The resulting linear dynamics in which the controller should be designed are

$$\begin{pmatrix} \dot{z}_1 \\ \dot{z}_2 \\ \dot{z}_3 \\ \dot{z}_4 \end{pmatrix} = \begin{pmatrix} z_2 \\ v_1 \\ z_4 \\ v_2 \end{pmatrix} = \begin{pmatrix} \dot{v}_x \\ \frac{F_x}{m} \\ \dot{v}_z \\ \frac{F_z}{m} \end{pmatrix}. \tag{5.17}$$

The fictional control inputs $\vec{v}$ can be recalculated into the actual controls through relation

$$\vec{u} = D^{-1} \cdot (\vec{v} - \vec{F}) \tag{5.18}$$

The described exact linearization scheme can be used to design a linear controller of the aircraft's airspeed and climb rate. The design naturally transitions into Mach hold system, described in section 4.5.2. More complicated is the transition to climb rate control, as described in section 4.5.1. The simplest way to combine the V_z control through the angle of attack and propeller commands is to use a similar serial connection of these two systems, similar to the combination of control surfaces and propeller for torque control, shown in Figure 5.1. The resulting system's architecture is shown in Figure 5.2.

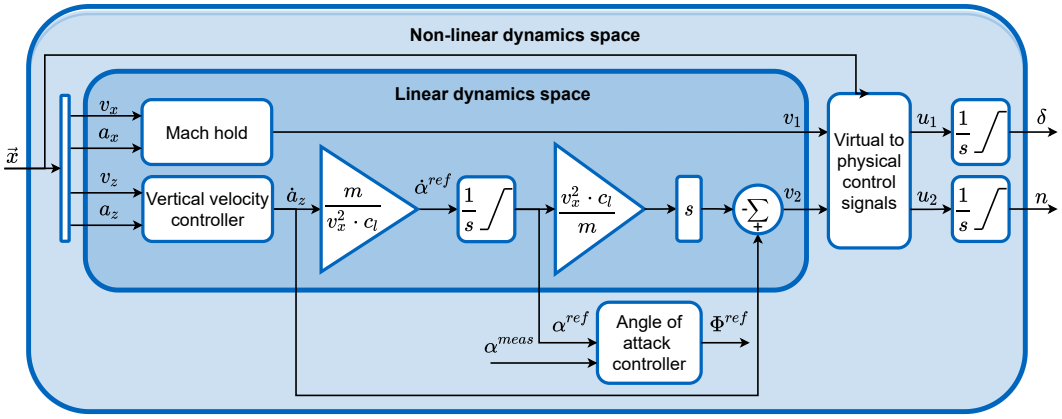

Figure 5.2. The architecture of velocity level control law, based on exact linearization and capable of VTOL maneuvers.

Both Mach and V_z hold systems can be designed as full state feedback architecture. Both controlled systems are represented as two integrator dynamics. The main issue with the design is the measurement noise of the states and physical limitations of the tilting speed and propeller's rotational acceleration.

Another issue is that the system can leave the safe flight envelope, as shown in Figure 3.9, due to insufficient tilt angle. Such a situation can, for example, happen if the aircraft attempts to slow down below stall speed and the wind-up situation occurs in the Mach hold controller. The result of this situation is that the tilt angle would stay zero even below the stall speed, and the aircraft would not be capable to keep zero vertical velocity. To prevent this, a saturation of the tilt angles to keep the maximal load factor available at least one or larger should be implemented.

5.4 Summary

This chapter has expanded on the fly-by-wire system for traditional aircraft and added VTOL capabilities for general tilt-rotor plane design. The main changes have been the addition of complete torque control through thrust vectoring of the propellers. The design uses real-time local linearization for the propeller's dynamics, combined with the original aerodynamic surfaces-based system. This design ensures consistent and complete controllability during the entire flight envelope. The rate and attitude control systems have not been modified due to the torque-based design. The velocity level capabilities have expanded with exact linearization of the dynamics between the propeller's thrust vectoring, and the aircraft's airspeed and the climb rate. The method linearized the aircraft dynamics and allowed consistent and predictable plane behavior during the entire flight envelope.

Chapter 6
VTOL Drone platform

The eVTOL vehicle for which was the fly-by-wire system developed is shown in Figure 6.1. The mechanical part of the design was done by Ing. Filip Tomáš and is not part of this thesis. This chapter focuses on measuring the drone parameters, the analysis of the system's expected dynamics, and finally, the parametrization of the fly-by-wire systems.

Figure 6.1. The eVTOL drone, designed by Ing. Filip Tomáš, that has been used for verification of the control algorithms.

6.1 Center of gravity and moments of inertia

The first step is to localize the aircraft's center of gravity and compute the moments of inertia. These measurements have been done mainly by Ing. Filip Tomáš and will not be described in detail.

The longitudinal and lateral position of CG can be calculated from the load on each aircraft wheel. The sum of torque moments generated from wheel loading must equal zero for both the x and z-axis, which leads to a set of linear equations. The measurement of CG's vertical position requires a different approach, as the aircraft has no practical point above CG that can be used to carry the aircraft load. Instead, simple suspension stability test, based on the geometry described in section 3.5, can determine the CG_z value. The aircraft is pitched up, with both rear wheels in contact with the ground. The pitch angle, for which the configuration is balanced, is found. The resulting relation between the pitch angle, the longitudinal distance between rear wheels and CG L_x^{wr} and the CG distance from the ground L_z^{wr} is

$$L_z^{wr} = L_x^{wr} \cdot \tan(\frac{\pi}{2} - \Theta). \tag{6.1}$$

The measurement of the aircraft's inertia was done using the pendulum method, described for example in [28].The experimental setup is shown in appendix B.1.

This measurement was only used to estimate the diagonal members of the inertia matrix, while off-diagonal ones were considered negligible. The measured values were provided with ±40 mm accuracy for the position of CG and ± 1.5% for the inertia matrix.

6.2 Propellers

The aircraft uses eight propellers for its propulsion, which are not evenly distributed around the aircraft CG. The position of propellers in hover configuration is shown in Figure 6.2. The front propellers have 22 inches (0.5588 m), whereas the rear ones have 16 inches (0.4064 m) in diameter. Unfortunately, the design has significant overlap between neighboring propellers. This issue limits the accuracy of thrust estimation.

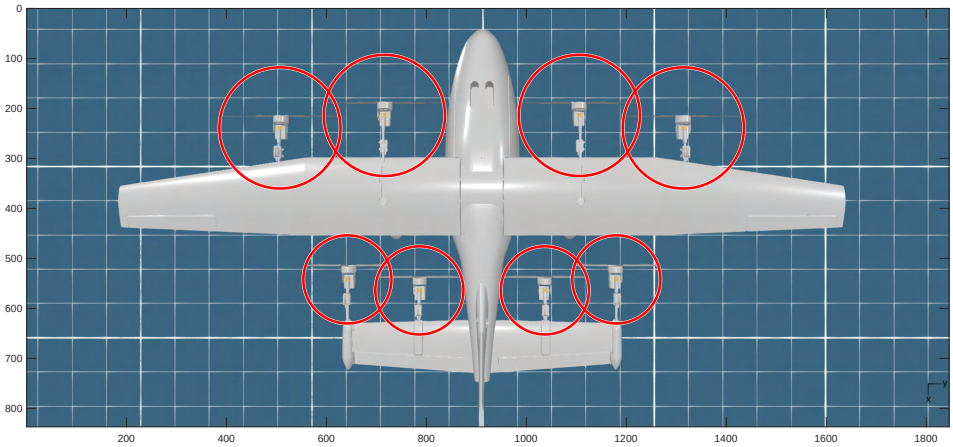

Figure 6.2. The description of propellers position in hover configuration.

It should be mentioned that the propeller's ESC system does not allow for direct speed control. Instead, the input variable is thrust command, which is approximately linear to propeller speed, especially in high-speed regions.

6.2.1 Wind tunnel testing

The torque and thrust values have been estimated according to equations (3.16) and (3.19). These equations are useful as all propellers have nearly identical pitch angles but different diameters. Both propeller types are designed for hover and have pitch angle of approximately 6 degrees. Section 3.4.1 describes the propeller's pitch angle and its influence on the propeller's thrust. Such an angle is outside the typical values used for aircraft, as shown in Figure 3.4. As no previous analysis could be found, the propellers have been tested in a wind tunnel to estimate their parameters. The experiment setup is shown in Figure 6.3.

Figure 6.3. The experimental setup for wind tunnel based propeller parameters estimation.

The wind tunnel size did not allow to measure the larger, 22-inch propeller, only the smaller 16-inch one. The pitch difference between the two propellers is only 0.5 degrees, which is negligible, and the following parameters can be used for the 22-inch propeller as well.

The propeller thrust, torque, and rotational speed have been measured for airspeed ranging from 8 to 28 m·s^{-1}. These values were then recalculated into non-dimensional parameters according to equations (3.12) to (3.15) and compared with current advance radio, calculated according to equation (3.10). The results are shown in Figure 6.4.

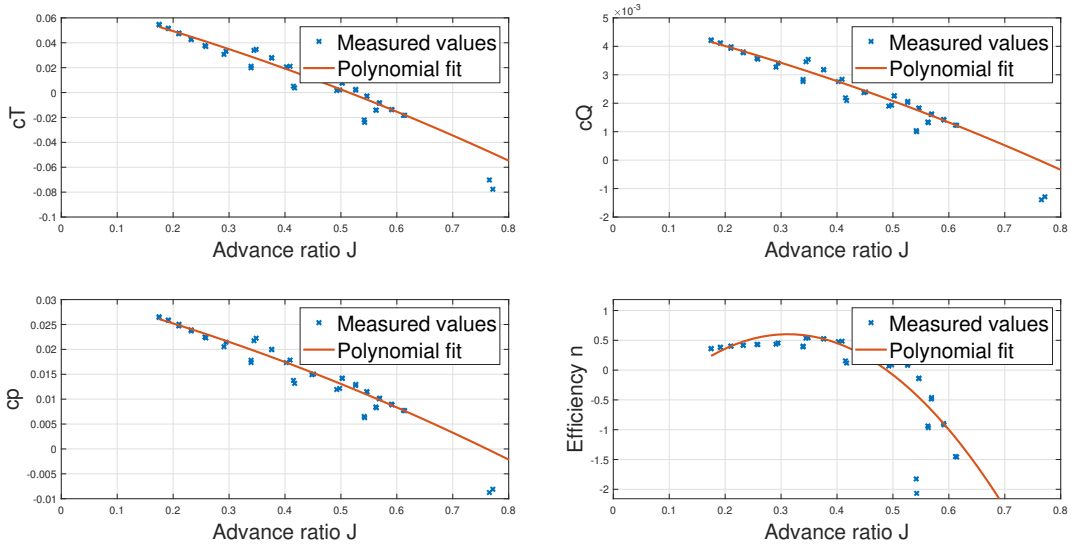

Figure 6.4. Parameters of the 16-inch propellers, measured in the wind tunnel.

It should be noted that the propellers can only generate thrust up to $J \approx 0.5716$. Due to limited power and maximal achievable engine speed, the propeller can not provide thrust above $v_\infty \approx 28$ m·s^{-1}. The relation between maximal achievable thrust and the minimal achievable advance ratio is shown in Figure 6.5. The relation between v_∞ and $J_{min}(v_\infty)$ and $T_{max}(v_\infty)$ can be considered linear.

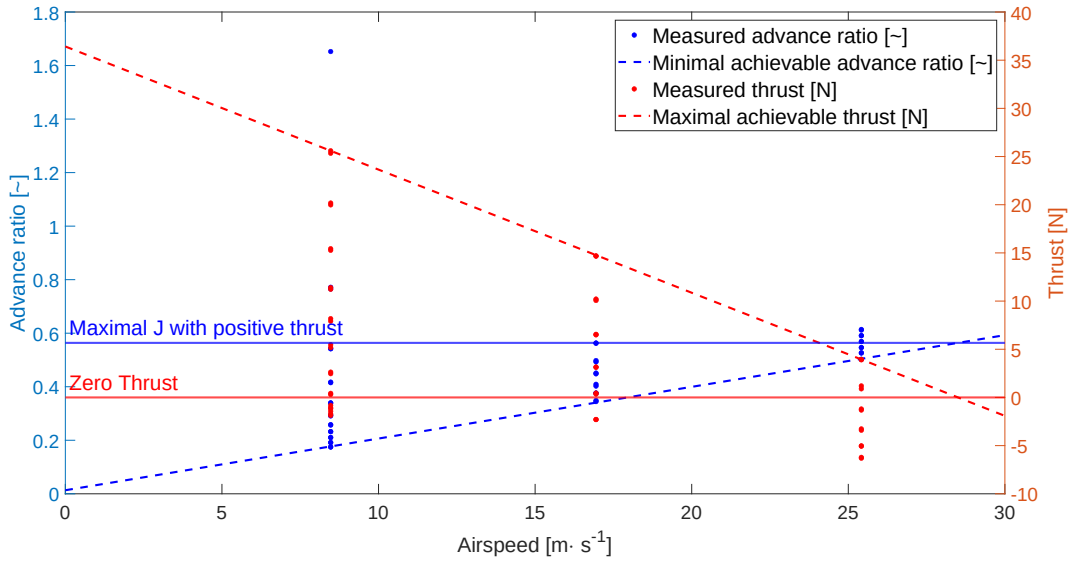

Figure 6.5. The comparison of maximal available thrust and minimal achievable advance ratio with respect to aircraft airspeed.

6.3 Airframe aerodynamic coefficients

The aerodynamic coefficients were determined using `OpenVPS` open-source software, developed by NASA. The analysis of the drone airframe was done by Ing. Marek Jalůvka and is not part of this thesis. The methods used to determine the airframe parameters do not include the influence of the propellers on the airframe. Due to this limitation, the results can differ significantly from the actual aircraft behavior.

Notably, the aircraft is expected to be stable in all flight configurations, allowing for manual control during flight mode. The airframe stall speed, calculated as

$$v_{stall} = \sqrt{\frac{2 \cdot m \cdot g}{\rho \cdot A \cdot C_L^{max}}} \tag{6.2}$$

is approximately 19 $\mathrm{m{\cdot}s^{-1}}$ or 68.4 $\mathrm{km{\cdot}h^{-1}}$. The minimal maneuvering speed, as described in section 3.11 is 22.8 $\mathrm{m{\cdot}s^{-1}}$. A maximal maneuvering speed can be considered the velocity, at which the aircraft is still capable to climb at least 2 $\mathrm{m{\cdot}s^{-1}}$. The maximal climb rate can be approximated as

$$v_z^{max}(v_\infty) = \frac{v_\infty \cdot (T_{avail}(v_\infty) - T_{req}(v_\infty))}{m \cdot g}, \tag{6.3}$$

where $T_{avail}(v_\infty)$ is the overall available thrust from all propellers, whereas $T_{req}(v_\infty)$ is the drag generated by the aircraft in horizontal flight. The part of $T_{avail}(v_\infty)$ from the rear 16-inch propellers can be simply calculated as four times the maximal achievable thrust from Figure 6.4. The front propeller's thrust must consider their different diameter and propeller speed. The advance ratio for given speed changes as

$$J_{22} = J_{16} \frac{n_{16}^{max} \cdot D_{16}}{n_{22}^{max} \cdot D_{22}} \approx 0.93 \cdot J_{16}. \tag{6.4}$$

The thrust for the same advance ratio should change according to

$$T_{22}(J) = T_{16}(J) \frac{(n_{22}^{max})^2 \cdot D_{22}^4}{(n_{16}^{max})^2 \cdot D_{16}^4} \approx 2.1738 \cdot T_{16}(J). \tag{6.5}$$

With these modifications, the resulting comparison between $T_{avail}(v_\infty)$ and $T_{req}(v_\infty)$ is shown in Figure 6.6. The maximal maneuvering speed is approximately 26 $\mathrm{m{\cdot}s^{-1}}$.

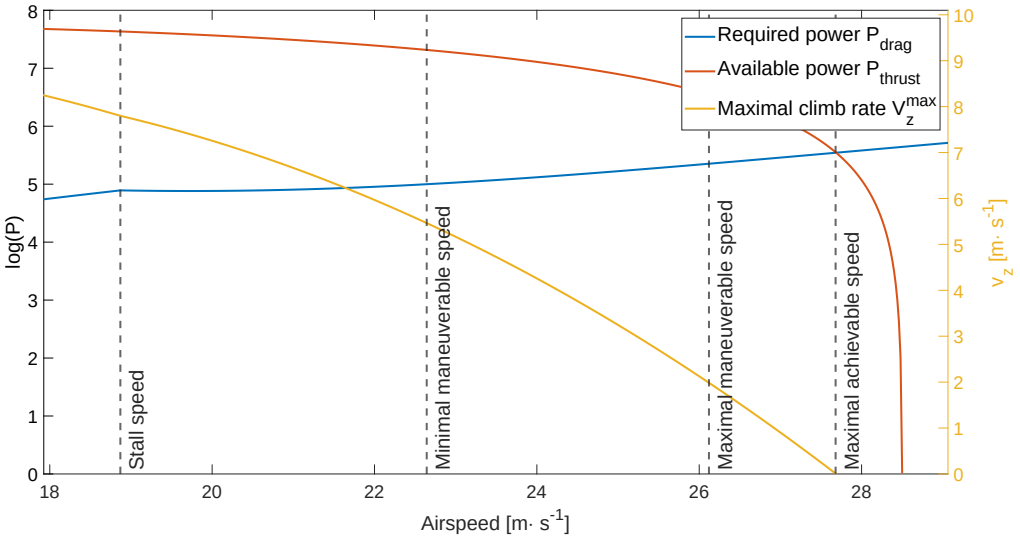

Figure 6.6. Comparison of available thrust and expected drag of the aircraft, combined with calculated V_z^{max} and the main aircraft velocities.

6.4 V-η Flight envelope

The combination of the propeller and aerodynamic data allows the analysis of aircraft's V-η flight envelope, including the region below stall speed. The basic analysis is described in section 3.11, however the equations (3.50) and (3.51) should be modified to include the actual propeller thrust, as described in Figure 6.5, and airframe drag. The modified relations are

$$\delta_{min}(v) = \arcsin\left(\frac{v_{stall}^2 - v^2}{v_{stall}^2 \cdot T_{avail}(v, \delta_{min}(v))}\right) \tag{6.6}$$

$$\delta_{max}(v) = \arcsin\left(\frac{T_{req}}{T_{avail}(v, \delta_{max}(v))}\right), \tag{6.7}$$

where $T_{avail}(v, \delta(v))$ depends not only on the current airspeed, but also on the tilt angle. This phenomenon is mentioned in section 3.4.1. The v_∞ is distributed between $v_{stream} = \cos(\delta) \cdot v$ and $v_{||} = \sin(\delta) \cdot v$, while only v_{stream} influences on the propeller's thrust value. The simplest way to solve the described equations seems to be usage of iterative methods. The resulting flight envelope is shown in Figure 6.7.

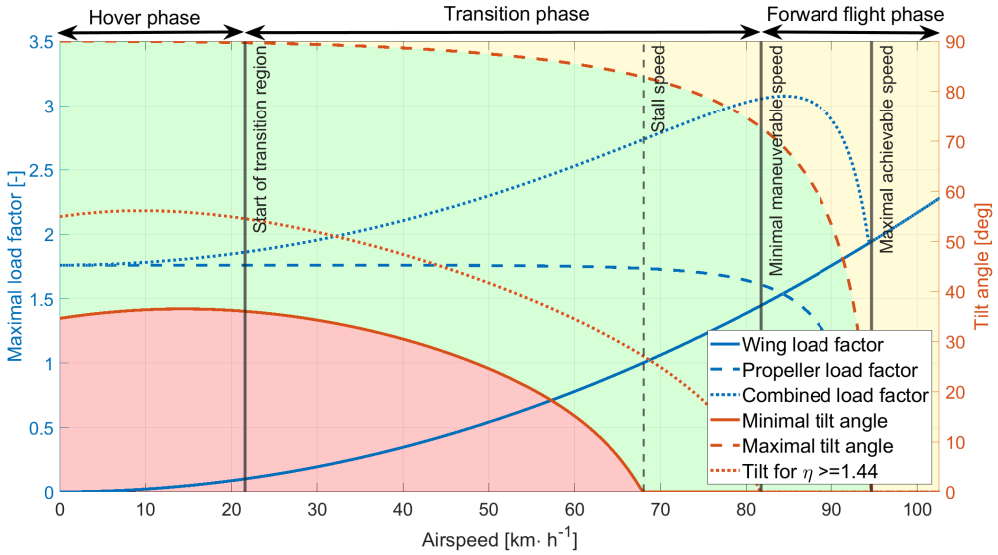

Figure 6.7. Complete flight envelope of the drone system.

Interestingly, the aircraft should be capable of reaching stall speed and even minimal maneuvering speed with a tilt angle above 70 degrees. However, such a configuration would increase the maximal load factor up to $\eta = 3$ and be well above $\eta = 1$, even with zero wing load factor. Therefore, the expected tilt angles for horizontal flight are below this maximal tilt angle line. The aircraft should, if possible, stay above the line Tilt for $\eta = 1.44$, as this region allows for sufficient maneuverability during the entire flight.

6.5 Electronic equipment

Onboard instrumentation consists of two independent flight computers (FC), one of which is used as a backup, and onboard sensors, namely IMU, pitot tube, GPS, barometer, and wind-vane probe sensor. The GPS measurement is not used for flight control. It is only used for tracking the aircraft flight trajectory. For this reason, it will not be described in this thesis.

FC and IMU system

The FC hardware utilizes the `TI_F38379D` board, which allows for direct implementation of Simulink code through the Embedded Coder Support Package. This ability to directly use Simulink code allows for simple Software-in-the-loop tests, complemented by the mathematical description of the aircraft dynamics. Unfortunately, the system does not ensure hard real-time implementation of the control algorithms. Meaning, the fly-by-wire can not utilize the computing power to its maximum potential, and therefore must reduce the update frequency of its feedback loop. Through experimental testing was the maximal update rate, which ensures the system's hard real-time behavior, determined to be 100 Hz.

The `BOOSTXL-SENSORS Sensors BoosterPack Plug-in Module` was added to the `TI_F38379D` board to provide accelerometer and gyroscope measurements. These values were then used as inputs into the AHRS filter, implemented by Ing. Marek Jalůvka. The filter's outputs are

- Euler angles $\begin{pmatrix}\Phi\\ \Theta\end{pmatrix} + \begin{pmatrix}e_\Phi\\ e_\Theta\end{pmatrix}$ [rad], where $\begin{pmatrix}e_\Phi\\ e_\Theta\end{pmatrix} \approx N(\begin{pmatrix}0\\0\end{pmatrix}, \mathrm{diag}(\begin{pmatrix}2.013\\9.682\end{pmatrix}))$ [μrad]
- Body rates $\vec{\omega} + \vec{e}_\omega$ [rad·s^{-1}], where $\vec{e}_\omega \approx= N(\begin{pmatrix}0\\0\\0\end{pmatrix}, \mathrm{diag}(\begin{pmatrix}1.784\\0.683\\0.973\end{pmatrix}))$ [μrad·s^{-1}]
- Body acceleration $\vec{a} + \vec{e}_a$ [m·s^{-2}], where $\vec{e}_a \approx N(\begin{pmatrix}0\\0\\0\end{pmatrix}, \mathrm{diag}(\begin{pmatrix}99.2\\124.3\\196.0\end{pmatrix}))$ [μm·s^{-2}]

Air-data and altitude sensors

The aircraft has two systems for air data and one for attitude measurements

- Pitot tube, measuring $v_\infty + e_v$, where $e_v \approx N(0, 33.2612)$ [m·s^{-1}]
- Wind-vane probe, measuring local α with accuracy 0.004 [rad] for $v_\infty > 11$ m·s^{-1}
- Barometer, measuring altitude [m] with additive noise $e_{alt} \approx N(0, 1.2015)$ [m] and measurement drift ≈ 2 mm·s^{-1}

The noise of the pitot tube is quite problematic. If we use the raw variance value, the minimal airspeed, at which the control surfaces can be safely used is according to equation (4.5) approximately 34.8 m·s^{-1} for $n_\sigma = 3$ and $E_{max} = 2$. This value is not acceptable, as it would not allow control of the aircraft with aerodynamic surfaces during any achievable flight phase. The noise must be reduced to $R_{filt} \approx 0.48$ to allow the usage of aerodynamic surfaces during the entire transition phase. The simplest way to reduce the noise is using a moving average filter of length n. The filter length can be calculated as $n = \frac{R}{R_{filt}} \approx 71$. The filter can be implemented as 1st order LP filter with a rise time of 0.45 seconds.

6.6 Fly-by-wire system setup

With a complete analysis of the aircraft's capabilities, the fly-by-wire system can now be parameterized. The rest of the chapter focuses on the parametrization of individual control loops, described in Chapters 4 and 5.

Filtering the natural frequencies of the mechanical structure

One of the main differences between the described mathematical model and actual aircraft is its structural stiffness. The model assumes rigid body behavior, which does not reflect the aircraft's flexible structures, mainly the wing. If the actuators induce any structural resonance frequencies, their amplitude will be amplified. The resulting oscillations make the aircraft uncontrollable and can even damage its structure.

Two natural frequencies were experimentally found during ground testing. The first frequency, located at 6.5 ± 0.5 [Hz] is induced by M_x torque generated by the actuators. The second is located at 9 ± 1 [Hz] and induced by M_y torque.

In order to prevent the induction of these frequencies, a band-stop filter should be implemented. The simplest design would be a continuous notch filter

$$\mathrm{H}_{notch}(s) = \frac{s^2 + f_{stop}^2}{s^2 + 2 \cdot f_{stop} \cdot s + f_{stop}^2}, \tag{6.8}$$

where f_{stop} [rad] represents the filtered frequency. Unfortunately, the discrete form of notch filter does not filter the required frequencies with sufficient dampening due to the limited sampling rate. Another option is the usage of a delay transfer function

$$\mathrm{H}_{delay}(s) = 0.5 \cdot (a + b \cdot e^{-\frac{s}{2 \cdot f_{stop}}}), \tag{6.9}$$

where parameters a and b define the band-stop filter shape. The design can be represented in discrete-time as a sum of delays, which allows for efficient implementation.

6.6.1 Rate level setup

The rate level controller design uses the fact that the aircraft is aerodynamically stable in cruise, which means that the system is least stable in hover. This configuration is also the easiest to describe. Therefore the hover setup is considered nominal, with aerodynamic stability and other uncertain parameters included in the robustness analysis. The nominal feedback system is shown in Figure 6.8.

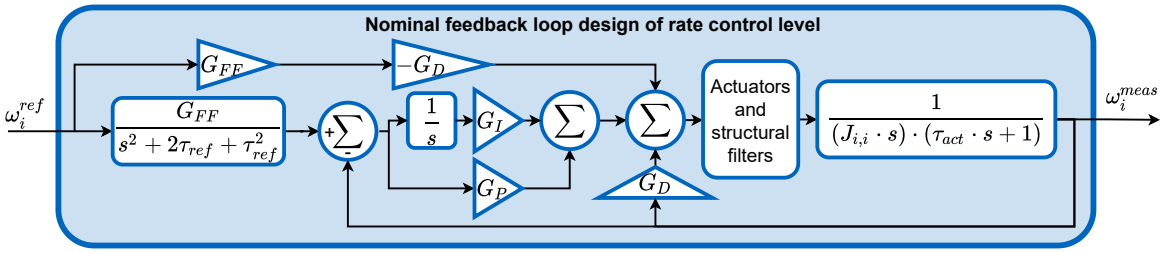

Figure 6.8. Nominal feedback design for rate level setup.

The controller's response requirements, given by the pilot, can be expressed as:

- Rise time faster than 0.25 s
- Overshoot smaller than 5 %
- Settling time at most 1 s
- Maximal command 90 deg $\cdot s^{-1}$

The parametrization of the nominal system was done using the response optimization toolbox, available in Matlab. The resulting system's robustness was analyzed for all known uncertainties.

Robustness analysis

The first step is to determine the controlled plant uncertainty created by:

- Moments of inertia
- Aerodynamic stability
- Actuators rise time
- Actuator level accuracy

Most of these uncertainties can be expressed as

$$W(s) > \frac{|G - G_0|}{|G_0|}, \tag{6.10}$$

matrix of filters, representing multiplicative uncertainty. However, the aerodynamic effect was not represented by $W(s)$, as the added stability significantly reduces the transfer function gain and unrealistically increases the robustness requirements. Instead, the damper gain G_D is scheduled according to the aircraft's airspeed to compensate for the aerodynamic stability effect. Uncertainty of the compensation is then included in the analysis. Figure 6.9 shows the resulting set of filters.

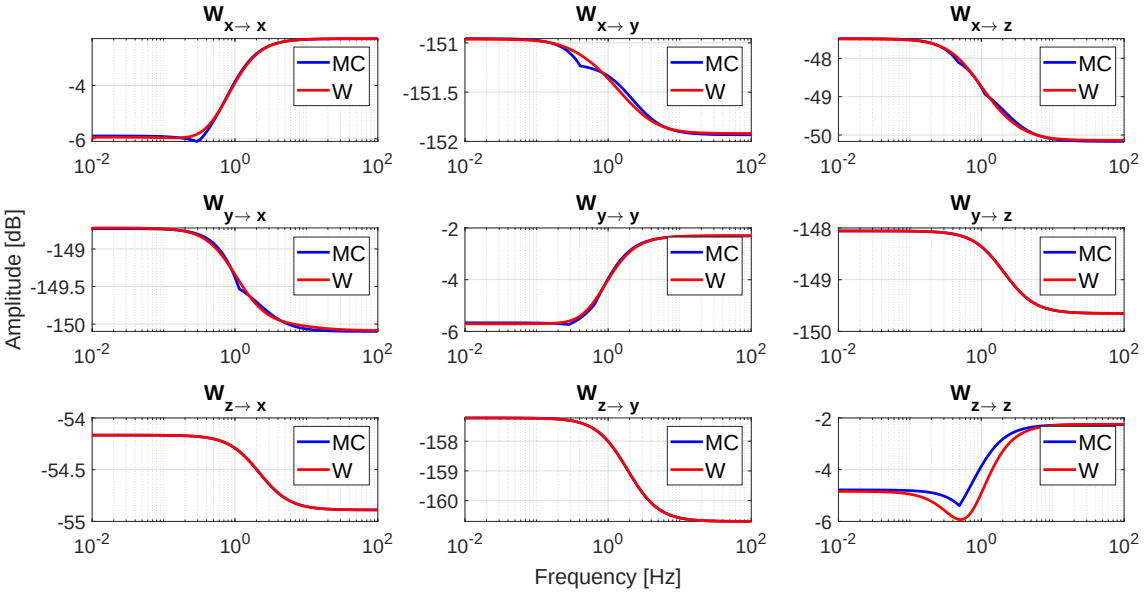

Figure 6.9. Multiplicative uncertainty of the rotational rates dynamics represented as second-order $W_{i\to j}(s)$ transfer function from i torque to j rate. MC represents the maximal value of Monte-Carlo simulations, whereas W represents the estimated uncertainty filter.

The control loop is robustly stable, if

$$||W \cdot T||_\infty \leq 1, \tag{6.11}$$

where T is the complementary transfer function. This h-infinity norm was calculated to be ≈ 0.58. The feedback loop is therefore considered robustly stable. As this analysis depends on the accurate estimation of the unknown, the traditional gain and phase margins of the open-loop system are also considered. These calculations used discretized form of the open-loop system to achieve more accurate results.

- Roll dynamics phase margin is 39.3 degrees and gain margin 10.71 dB.
- Pitch dynamics phase margin is 34.5 degrees and gain margin 10.04 dB.
- Yaw dynamics phase margin is ∞ degrees and gain margin 70.23 dB.

These values are above typical minimal stability requirements of 30 degrees phase and 6 dB gain margin. The system should be sufficiently robust to all considered uncertainties.

6.6.2 Attitude level setup

The regulator stabilizes the aircraft's roll and pitch angle dynamics. Unlike the rate level, the response can be significantly slower but must be without overshoot.

The feedback section is used only to control relatively slow dynamics, whereas the feed-forward section allows the pilot to quickly react through the rates command. This combination allows for robust feedback design without reducing the control bandwidth.

The feedback loop parameters were designed through the response optimization toolbox so that the overall system has no significant overshoot and rise time of approximately 0.4 seconds. The system without a feed-forward section has a rise time above one second.

Robustness analysis

The robustness analysis follows the same steps as in the previous design.

The estimation of uncertainty filter uses controlled rates and integrator dynamics. The resulting $W(s)$ filter for roll and pitch angle dynamics is shown in Figure 6.10. The diagonal filters $W_{x\to\Phi}$ and $W_{x\to\Theta}$ show the influence of the rate level feedback on the uncertainty for low frequencies.

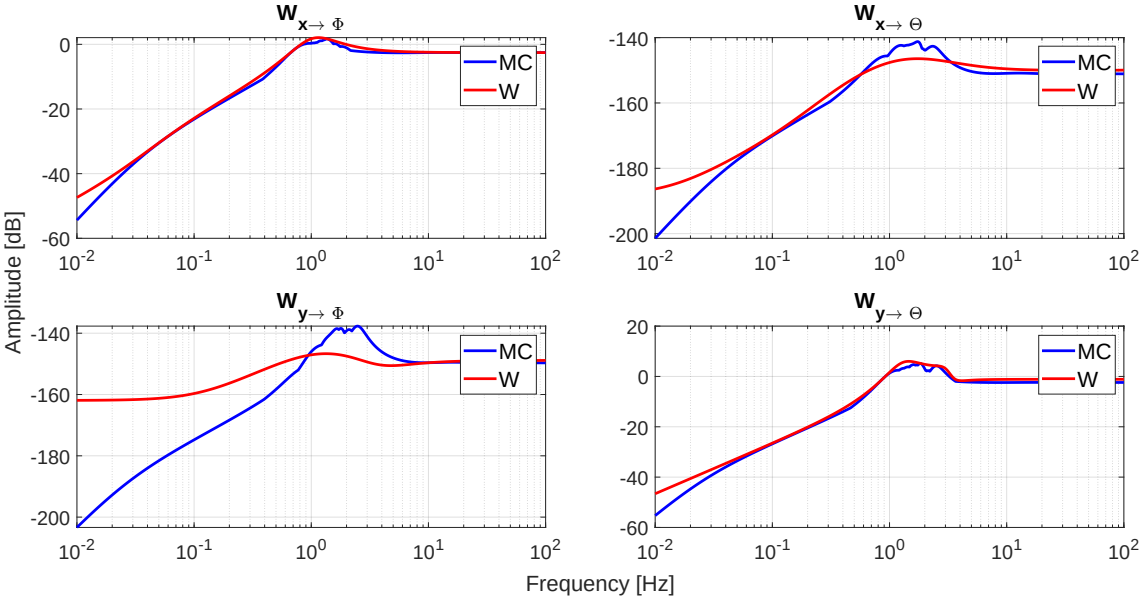

Figure 6.10. Multiplicative uncertainty of the attitude dynamics, represented as fourth-order $W_{i\to j}(s)$ transfer function from i rate command to j angle. MC represents the maximal value of Monte-Carlo simulations, whereas W represents the estimated uncertainty filter.

The uncertainty rises above 0dB at around 1.5 Hz for both filters. Therefore, the complementary feedback function -3dB bandwidth should end around at most 1.5 Hz. The designed system must not have overshoot and therefore is significantly slower.

The resulting attitude hold system has h-infinity norm $||W \cdot T||_\infty \approx 0.21$. The traditional stability margins are:

- Roll dynamics phase margin is 65.73 degrees and gain margin 12.09 dB.
- Pitch dynamics phase margin is 63.44 degrees and gain margin 11.89 dB.

The system has a significant stability margin and should be robustly stable at all considered configurations.

6.6.3 Velocity level setup

Because of the exact linearization design, the system is divided into three decoupled linear controllers. Each controller can be considered independent.

Mach hold setup

The linearized dynamics are

$$\begin{pmatrix} \dot{v}_x \\ \dot{a}_x \end{pmatrix} = \begin{pmatrix} 0 & 1 \\ 0 & 0 \end{pmatrix} \cdot \begin{pmatrix} v_x \\ a_x \end{pmatrix} + \begin{pmatrix} 0 \\ 1 \end{pmatrix} \cdot v, \tag{6.12}$$

where v is the control input. The system can be controlled using a full-state feedback LQR regulator. The v_x speed can be assumed to be identical to the v_∞ value, measured by the pitot tube. The approximation is based on the pitot tube's low directional sensitivity. The onboard accelerometer directly measures the value a_x.

However, even though all states are measured, the noise of the pitot tube would make the design of the LQR regulator challenging. To mitigate the noise issue, the measured data can be filtered using a state observer with Kalman gain. The combination of LQR and Kalman filter is typically described as an LQG controller.

The controller's performance was tested on simulated data with the following results

- Rise time of the v_x dynamics $\approx$ 2 s.
- Process noise of both v_x and a_x dynamics with variation $R_v \approx R_a \approx 0.3$ m·s^{-1}.

Unlike the LQR controller, which ensures robust stability with a minimal 6dB gain and 60 degrees phase margin [29], the LQG regulator does not provide such guarantees [29]. For this reason, robustness analysis should be included in the controller design. As the resulting open-loop system has a single input and multiple output (SIMO) structure, standard phase and gain margins are insufficient.

A more appropriate method for robustness analysis uses disk margin, with independent variations for the controlled plant inputs and outputs. The resulting disk margin is shown in Figure 6.11. The resulting stability margins are considered sufficient.

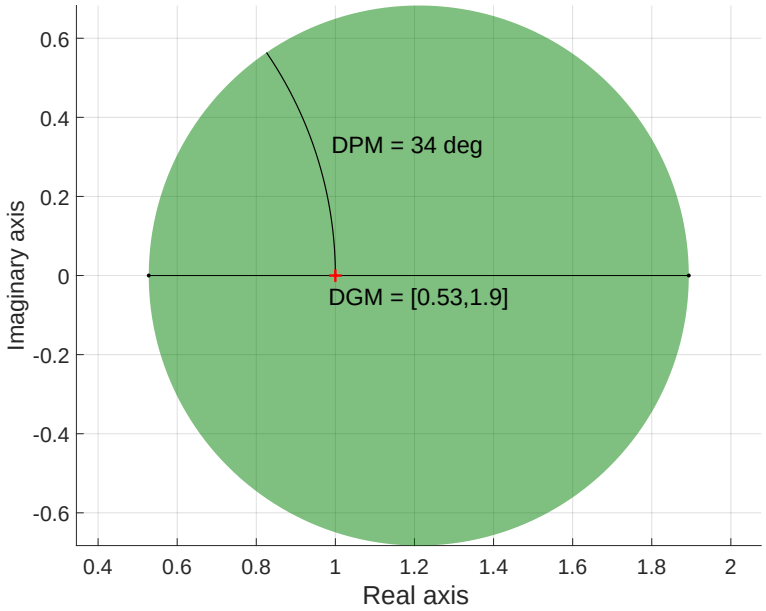

Figure 6.11. Disk margin for Mach hold controller in the complex plane with disk phase margin 34 degrees and disk gain margin 5.5 dB.

Vz hold setup

The linearized dynamics are identical to the Mach hold case. However, the aircraft's onboard sensors cannot measure v_z. The system instead measures the aircraft altitude p_z through a barometer sensor. This forces the expansion of the controlled model into triple integrator dynamics

$$\begin{pmatrix} \dot{p}_z \\ \dot{v}_z \\ \dot{a}_z \end{pmatrix} = \begin{pmatrix} 0 & 1 & 0 \\ 0 & 0 & 1 \\ 0 & 0 & 0 \end{pmatrix} \cdot \begin{pmatrix} p_z \\ v_z \\ a_z \end{pmatrix} + \begin{pmatrix} 0 \\ 0 \\ 1 \end{pmatrix} \cdot v, \tag{6.13}$$

where v is again the control input. Inclusion of the altitude to the Vz hold controller requires modification of the input signal. The pilot's command can not reference only the v_z signal but must also include a reference for p_z. This can be achieved by integrating the v_z^{ref} to p_z^{ref}.

The controlled attitude dynamics include additional integrator. Therefore the system is capable to track ramp p_z^{ref} and step v_z^{ref} without a steady-state error.

The barometers are not as noisy as pitot tubes but are known to have significant rise time. However, this parameter is unknown and increases the robustness requirements for the overall design. The Loop Transfer Recovery (LTR) heuristic approach was used to increase the regulator's stability margins. The resulting disk margin is shown in Figure 6.12. The values approach the margins of the LGR controller and are considered sufficient.

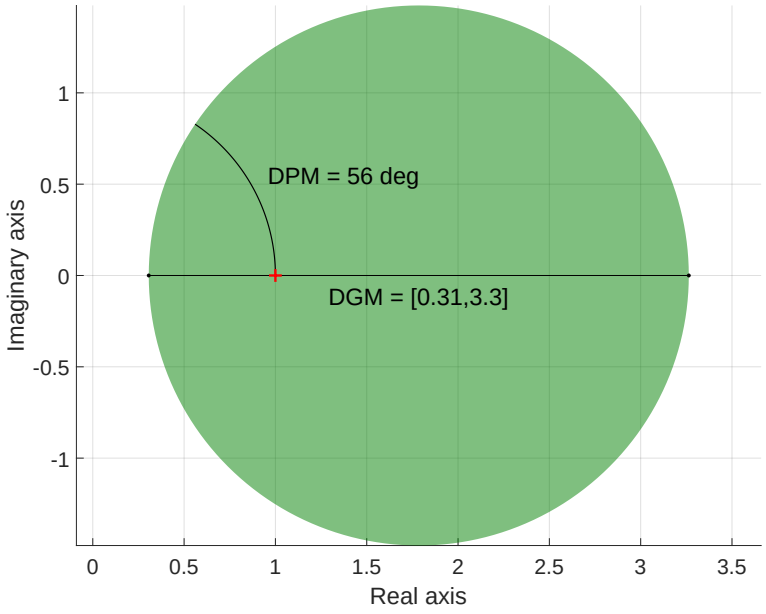

Figure 6.12. Disk margin for the Vz hold controller in the complex plane with disk phase margin 56 degrees and disk gain margin 10.4 dB.

The system performance was tested with the same method as the Mach hold controller. The resulting dynamics are

- Rise time of the v_z dynamics ≈ 0.9 s.
- Noise of the controlled states $R_p \approx 3.8$ mm , $R_v \approx 0.2$ mm·s^{-1}, $R_a \approx 1.2$ mm·s^{-2}

Angle of attack controller setup

The dynamics of the angle of attack can be simplified into a form

$$\begin{pmatrix} \dot{v}_z \\ \dot{\alpha} \end{pmatrix} = \begin{pmatrix} 0 & \frac{C_L}{m} \\ \frac{1}{vx} & -\frac{1}{\tau_\Theta} \end{pmatrix} \begin{pmatrix} v_z \\ \alpha \end{pmatrix} + \begin{pmatrix} 0 \\ \frac{1}{\tau_\Theta} \end{pmatrix} \cdot \Theta^{ref} \tag{6.14}$$

by linearizing the dynamics around $v_z \approx 0$ and assuming $\dot{v}_x \approx 0$. The τ_Φ parameter approximates the rise time of the pitch angle controller while

$$C_L \approx 0.5 \cdot \rho \cdot A \cdot v_x^2 \cdot \frac{dCl}{d\alpha}. \tag{6.15}$$

The dynamics are uncertain as v_x and τ_Φ change during the flight. The manufacturer guarantees the angle of attack sensor to provide accurate data only when the local airspeed is above $v_\infty \approx v_x > 11$ m·s^{-1}. The controller is therefore set up for flight speed above 13 m·s^{-1}. Bellow this minimal speed, the α is assumed to equal Θ.

The uncertainty of the controlled dynamics, combined with the derivative nature and the performance requirements, proved too complicated for the PI controller. Instead, a second-order h-infinity system was implemented. Figure 6.13 shows the frequency responses used for the controller design. The feedback loop step response is expected to have a steady-state gain between 0.92 and 0.96.

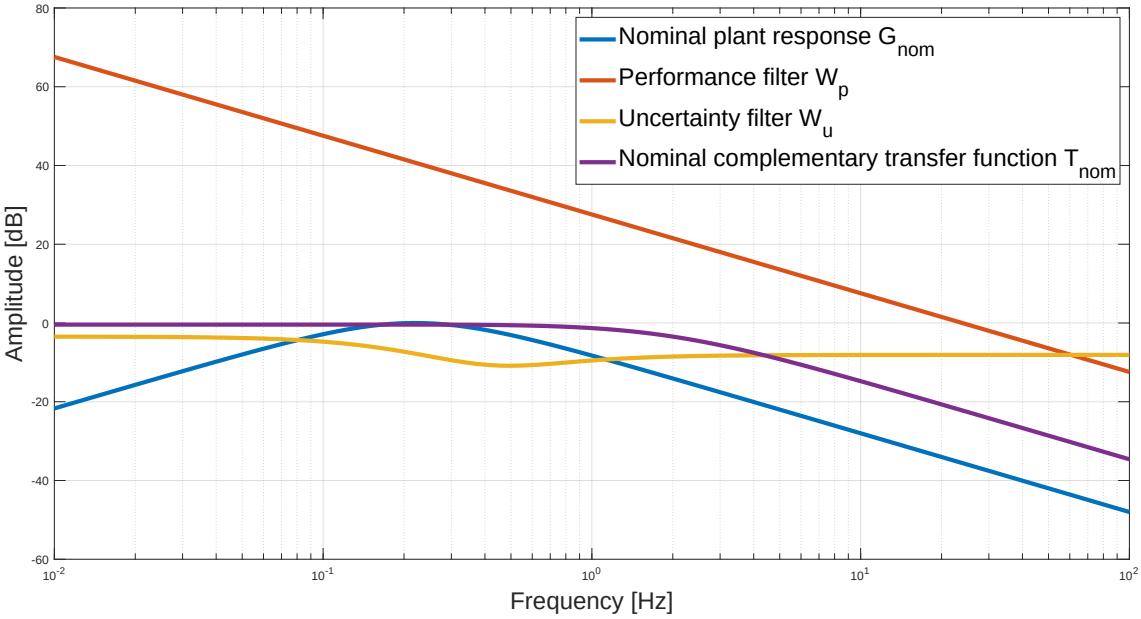

Figure 6.13. Frequency responses of angle of attack dynamics.

6.7 Summary

This chapter has described the implementation of general fly-by-wire architecture on a specific eVTOL drone. It included the analysis of the drone inertia, propellers, airframe performance, and onboard instrumentation. These parameters were then used for the robust setup of the individual control systems. Each system's robustness was verified either using the h-infinity norm or with a disk margin.

Chapter 7
Software in the loop simulations

In order to simulate the behavior of developed algorithms, a software-in-the-loop (SIL) approach was used. Due to the hardware's capability to deploy Simulink-based code, it can be verified in the Simulink program, where the mathematical model can be implemented as well. The model's responses were visualized in the `FlightGear` simulation program. The implementation of the experimental drone's 3D model into the simulator was done by Bc. Ondřej Procházka. The resulting visualization is shown in Figure 7.1.

Figure 7.1. Visualization in `FlightGear` simulation program.

The Simulink software also allows for a simple control panel implementation, as shown in Figure 7.2, that displays the aircraft state and allows for direct control of the aircraft, either through Simulink sliders or by connecting a joystick to the computer.

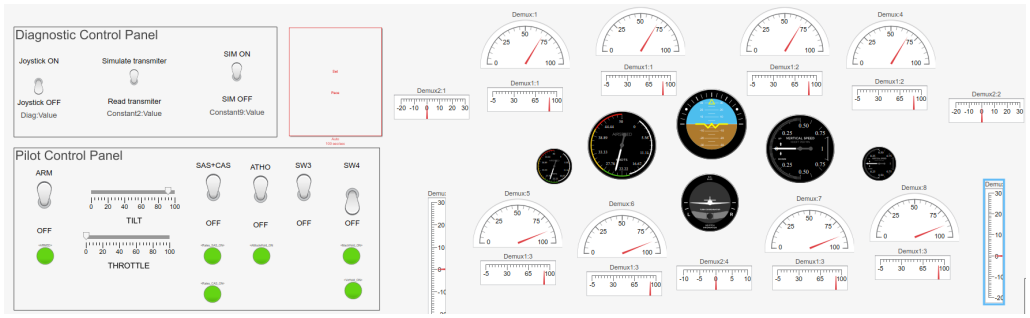

Figure 7.2. Control panel in Simulink, showing the aircraft state, engines thrust, tilt angles, position of the control surfaces, as well as logic switches.

The rest of the chapter uses the SIL system to verify the developed fly-by-wire algorithms through interactions with the mathematical model. Firstly, the lower-level systems are tested, followed by a simulated transition from hover to cruise that demonstrates the overall system's performance, including the interaction between individual control systems.

With the basic behavior confirmed, more complicated maneuvers are also simulated and discussed to demonstrate the aircraft's capabilities.

7.1 Response of the Rate level

Firstly, the rate level is tested. Figure 7.3 shows the simulated controller's step response for a hundred randomly sampled aircraft configurations. It should be noted that slower modes, which the higher-level control should compensate, are not included in these simulations.

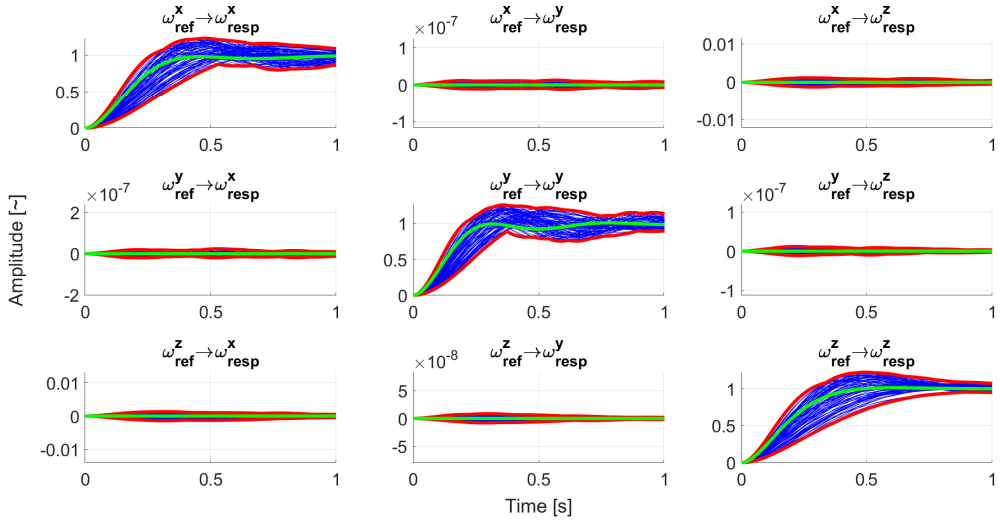

Figure 7.3. Rate level step response. The green line represents the nominal system.

These Monte-Carlo simulations show the robust performance of the designed algorithm. The cross-coupling effects are sufficiently damped, and the dynamics can be considered decoupled.

7.2 Response of the Attitude level

The attitude level response is simulated according to the same MC technique as the previous level. However, the simulations now include all modes of the aircraft.

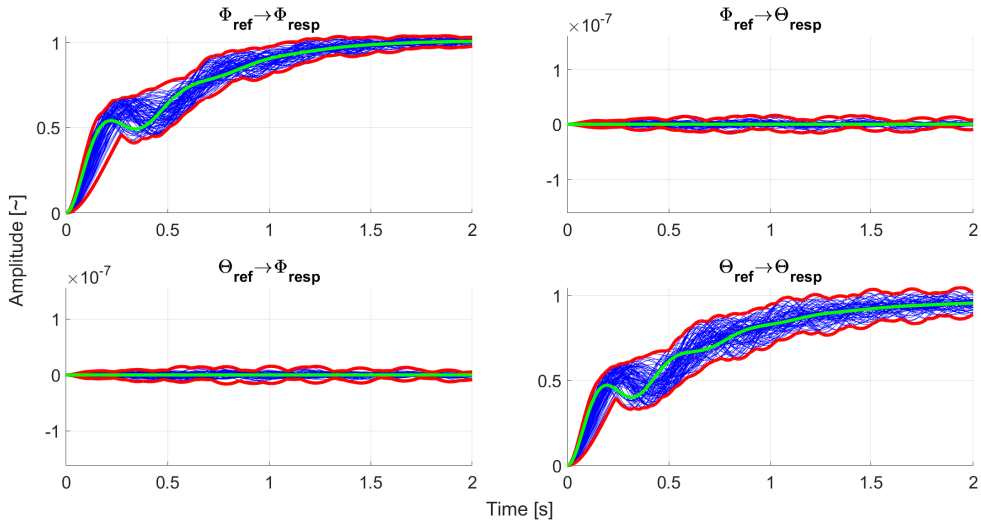

Figure 7.4. Attitude level step response. The green line represents the nominal system.

The responses show completely decoupled dynamics. The settling time is around two seconds. It should be noted that small oscillations can be seen during response rise. For this reason, the higher-level controller (or the pilot) should not request fast attitude changes, as it could lead to oscillations.

7.3 Transition from hover to cruise

The most important maneuver for VTOL aircraft is the transition from hover to cruise and back without significant loss in altitude. The pilot can change the reference airspeed from zero to the required value and then back to zero to execute the maneuver. The aircraft's airspeed and altitude responses are shown in Figure 7.5.

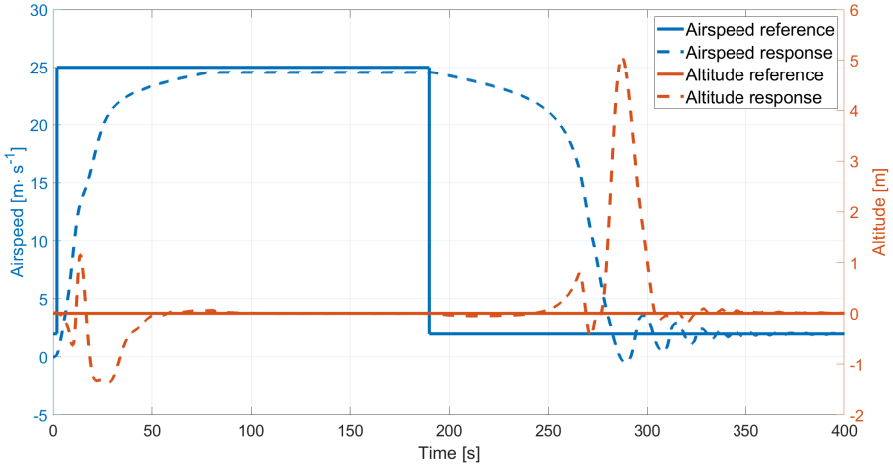

Figure 7.5. Aircraft velocities during basic transition maneuver.

The aircraft can reach the required maximal velocity without overshoot. This is mostly caused by the fact that the engines can no longer provide large excess of thrust at this airspeed. The aircraft keeps the current altitude with a maximal error of around one meter. The biggest error occurs, when the angle of attack system is activated and deactivated. The α-controller response is shown in Figure 7.6. The transition from cruise to hover shows significantly worse behavior, including overshoot, oscillation, and five meters loss of altitude.

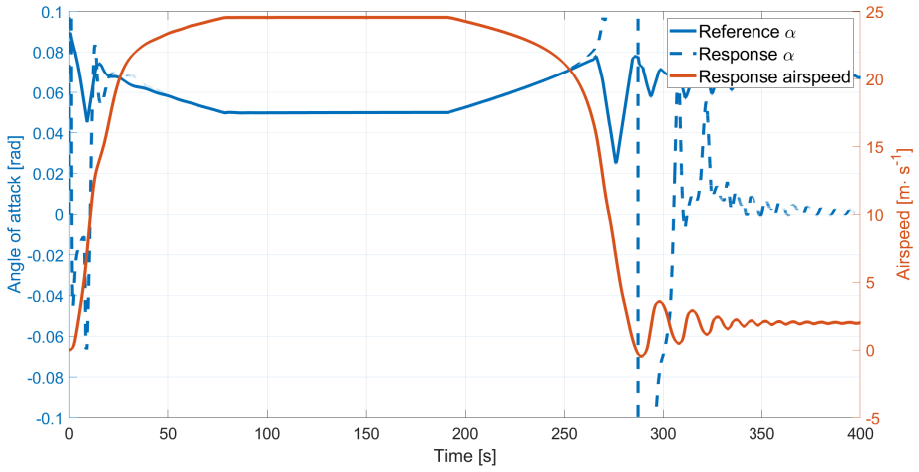

Figure 7.6. Aircraft angle of attack during basic transition maneuver.

The controller tracts the desired α^{ref} perfectly. This zero steady-state error is based on the fact that the aircraft is holding altitude. As long as vertical velocity $V_z \approx 0$, the α dynamics is approximately identical to the aircraft pitch angle Θ.

7.4 Transition during a coordinated turn

The previous maneuver requires a large area to be executed, which can be problematic. Instead, the aircraft can execute the transition during a coordinated turn. The plane accelerates to minimal speed for coordinated turn maneuver, which is well below stall speed, and then changes its bank angle to a non-zero value. The resulting maneuver, including the transition back to hover, is shown in Figure 7.7.

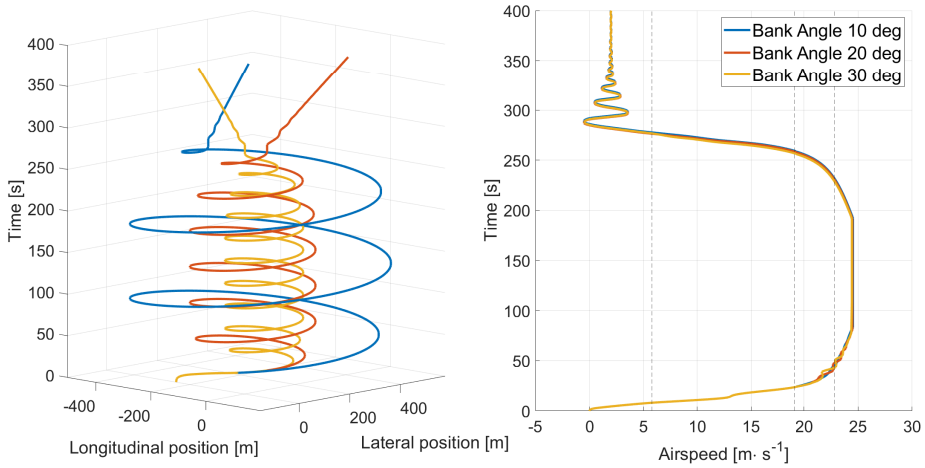

Figure 7.7. Aircraft position and airspeed for transitioning during a coordinated turn. Each line represents a different bank angle.

The figure clearly shows that the bank angle does not significantly affect the transition maneuver. The aircraft has sufficient excess of thrust to allow for a coordinated turn even below stall speed, which is not possible for traditional aircraft. The following Figure 7.8 shows the altitude change during the maneuver. The results are similar to the previous basic transition case.

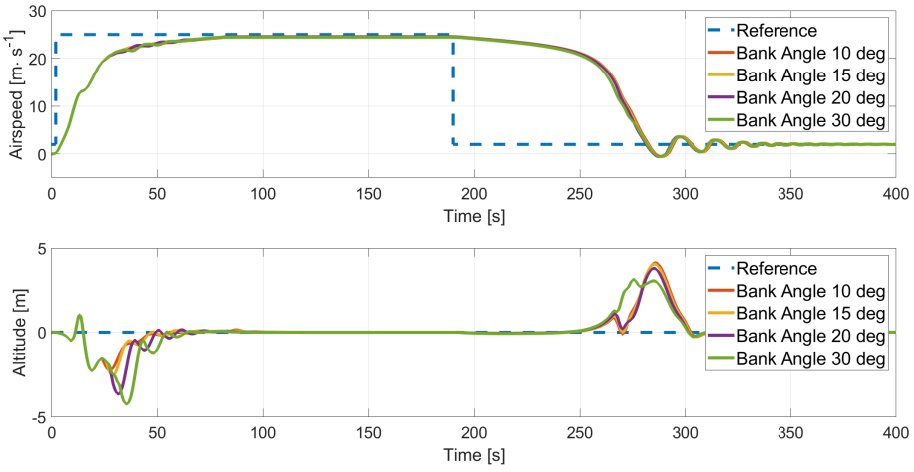

Figure 7.8. Aircraft vertical velocity and airspeed for transitioning during the coordinated turn for different bank angles.

7.5 Transition during a climb.

Another option is to transition when the aircraft climbs to a specific altitude. This type of maneuver would be especially useful in urban areas, where the plane must climb above the surrounding buildings and attempt to achieve cruise speed quickly. The maneuver was tested for three different climb references, as shown in Figure 7.9

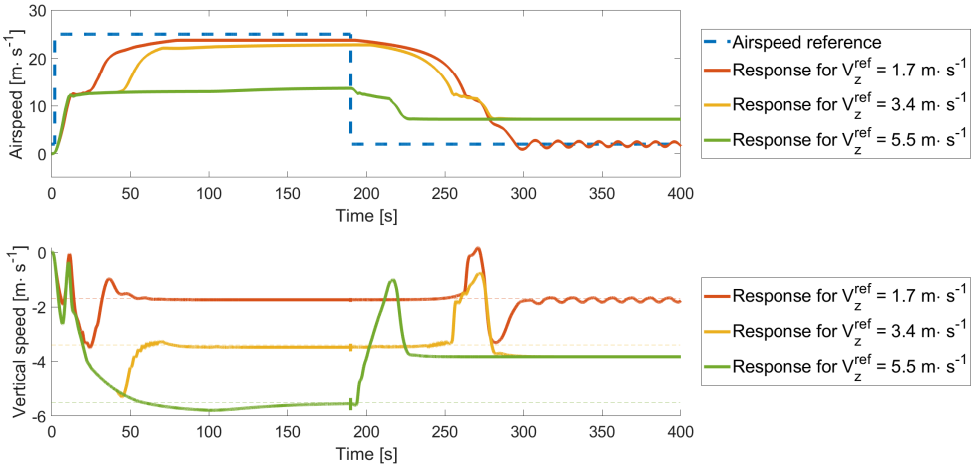

Figure 7.9. Aircraft vertical velocity and airspeed for transitioning during a climb.

Unlike the coordinated turn example, the climb significantly affects the controller performance. During the transition from hover to cruise, the activation of the α-controller causes larger errors than in the previous cases.

Furthermore, the aircraft is not capable of transitioning to cruise configuration when the required climb speed is above approximately 4 $\mathrm{m{\cdot}s^{-1}}$. An even greater problem is to reduce the airspeed back to hover from cruise mode. If the aircraft attempts to climb faster than 3 $\mathrm{m{\cdot}s^{-1}}$, it will not be able to reduce speed below approximately 7 $\mathrm{m{\cdot}s^{-1}}$.

The cause of the effect is not fully understood, but the answer would most likely include the mutual canceling of control commands from the MachHold and VzHold systems. This most likely happens when the control signals are transformed from linear to nonlinear control space. The described issues can also be demonstrated through the aircraft angles, as described in Figure 7.10.

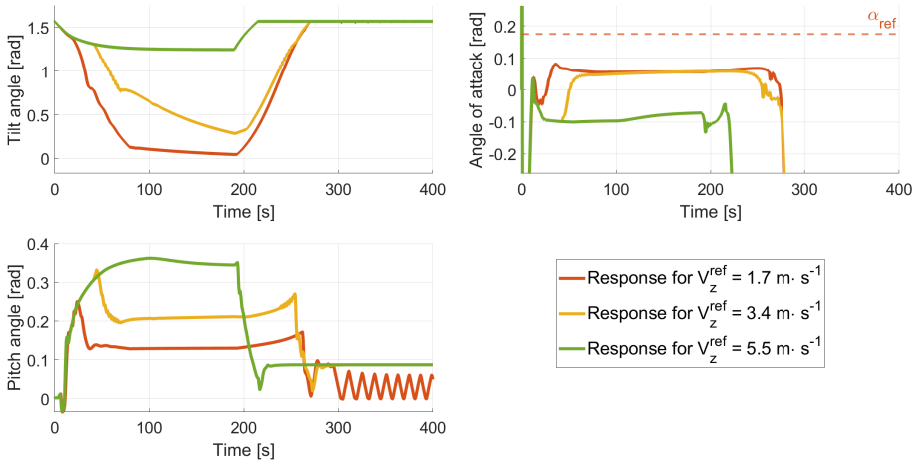

Figure 7.10. Aircraft angles δ, Θ and α for transitioning during a climb.

The tilt angle δ only approaches zero degrees for case V_z^{ref} =1.7 m·s^{-1}. In all other cases, the aircraft still uses the propellers to compensate for an insufficient lift from the wings. The lift is small because the α controller can not keep zero steady-state error.

These issues show that the system has some difficulties transitioning during the climb. The aircraft is still stable and controllable, so this problem is not considered critical.

7.6 Transition with noisy measurements

A considerable part of the Thesis is dedicated to analyzing robust stability and performance with noisy data sources. The most significant source of measurement noise is the pitot tube. The systems are designed to mitigate the noise influence. In order to verify this ability, the simulator was expanded with models of individual sensors and rigorously tested. An example representing the transition in horizontal flight is presented. Tracking of airspeed is shown in Figure 7.11.

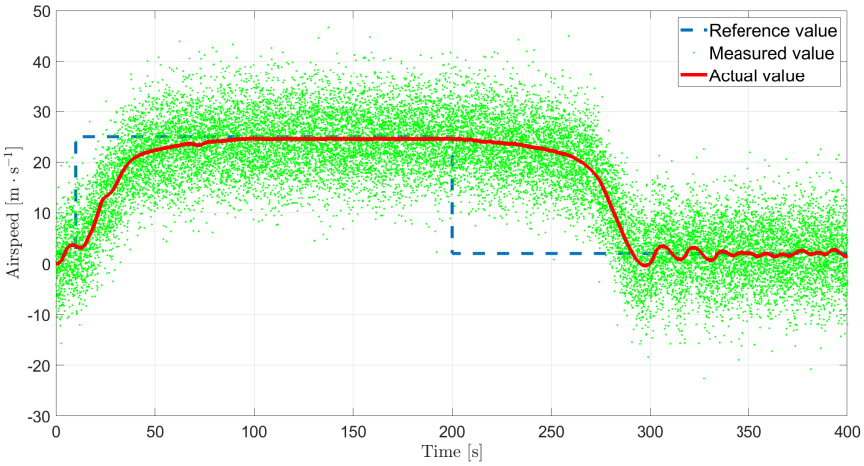

Figure 7.11. Aircraft airspeed response on noisy data inputs.

The system's response is nearly identical to the simulation without noise, depicted in Figure 7.5. The only noticeable difference is the algorithm's inability to keep zero steady-state error. The aircraft's airspeed slightly oscillates around the desired value. This behavior seems to be unavoidable for such a level of measurement noise. The vertical velocity response during transition is presented in Figure 7.12.

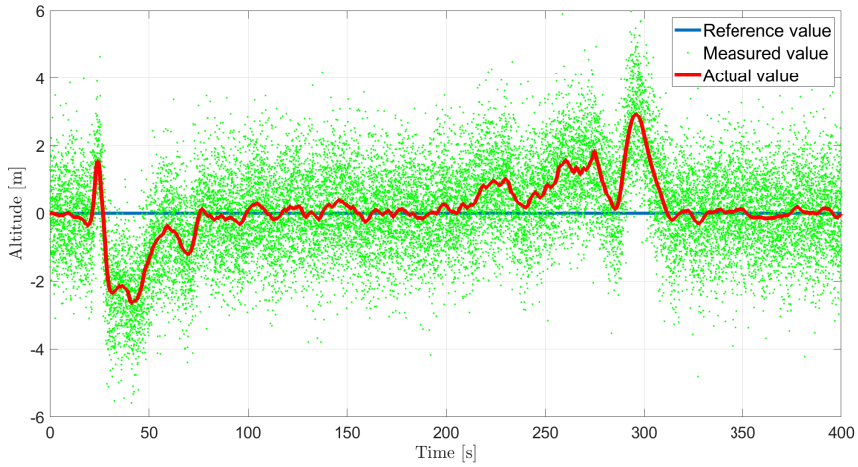

Figure 7.12. Aircraft vertical velocity response on noisy data inputs.

The system's behavior is again similar to the simulation without noise, as shown in Figure 7.5. The measurement noise does not affect the fly-by-wire system's capability to transition from hover to cruise mode.

The last analyzed signal reflects the usage of aerodynamics surfaces during flight. The actuator's level only uses the aerodynamics surfaces above certain airspeed, based on the measurement data, to ensure robust behavior.

As shown in Figure 7.13, the elevator is only used above 5 $\mathrm{m{\cdot}s^{-1}}$. Above this velocity, the error caused by inaccurate data is within the expected bounds, and the system remains stable.

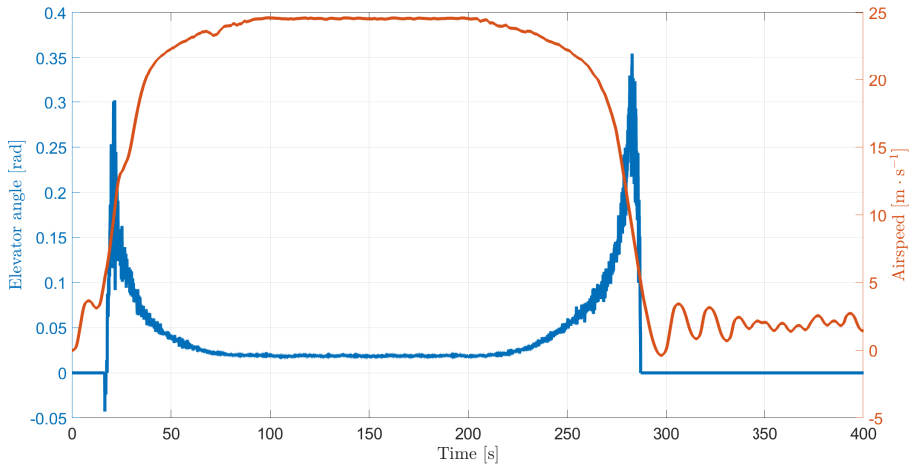

Figure 7.13. Aircraft elevator control commands.

7.7 Conclusion

The chapter described simulation-based verification of the developed algorithms. Simulator used `FlightGear` based visualization to interpret the aircraft behavior better.

The fly-by-wire system successfully demonstrated its ability to transition from hover to cruise mode in basic horizontal flight and during coordinated turns and small climbs. The system is not capable of transitioning during a significant climb. However, the aircraft remains stable and controllable.

Lastly, models of sensors were used to demonstrate the system's response to noisy measurements. Due to the filtering described in the Thesis, the system coped well with the measurement noise and did not significantly change performance during flight.

Chapter 8
Flight based testing and validation

The last step of the control approach validation is to carry out extensive flight tests. Unfortunately, every flight depends on many external factors, including the availability of an experienced pilot, operational aircraft, and great weather. These requirements severely limited the number of flight tests executed during the thesis writing. For this reason, only basic tests in hover configuration were conducted in time to be included in this text.

However, these results are still significant as the hover configuration is the least stable. Also, these basic flight tests are used to confirm the capability of the system to control an actual aircraft outside of simulations. The system demonstrated its capability to hover without many issues.

Two examples of the drone in flight are presented in Figures 8.1 and 8.2.

Figure 8.1. Drone during hover tests.

Figure 8.2. Drone during yaw control tests.

8.1 Rate level validation.

The first hover tests verified rate and actuator level control. Their main mission was to validate the system's parametrization based on the mathematical model.

The test began with short flights in hover, focused on validating the aircraft's controllability, followed by a pitch rate test. It involved pitching the aircraft up and down to accelerate itself forward and change its position a few meters ahead. The system's response is shown in Figure 8.3.

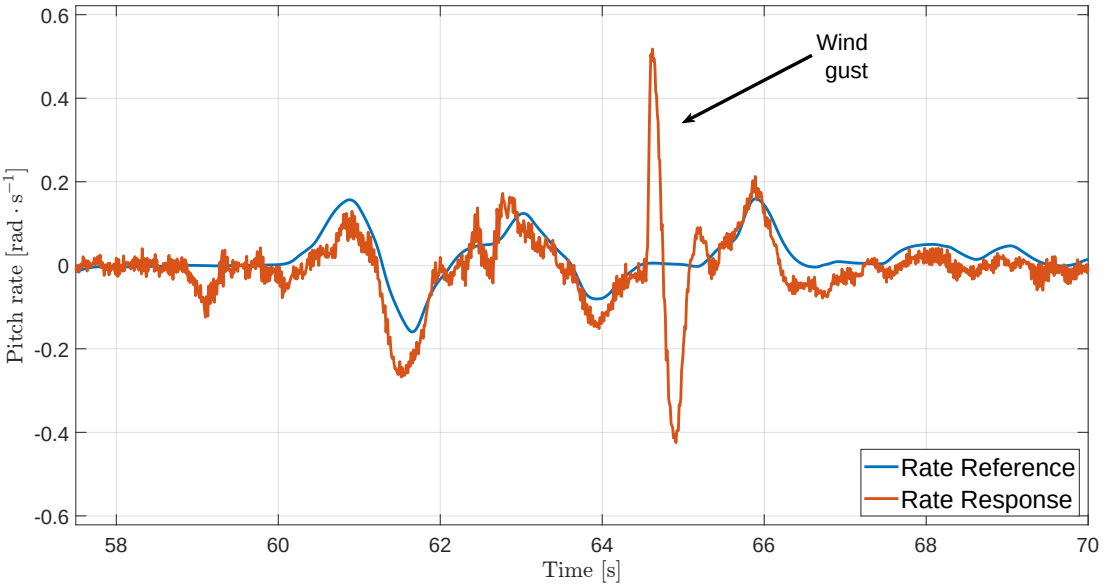

Figure 8.3. Pitch rate during low-speed maneuvering, including disturbance rejection.

The controller tracts the desired state quite well. The system does not show oscillations or significant overshoot. Interesting is the disturbance rejection, which is surprisingly fast. The behavior of roll and yaw rate controllers during the same maneuver is shown in Figure 8.4.

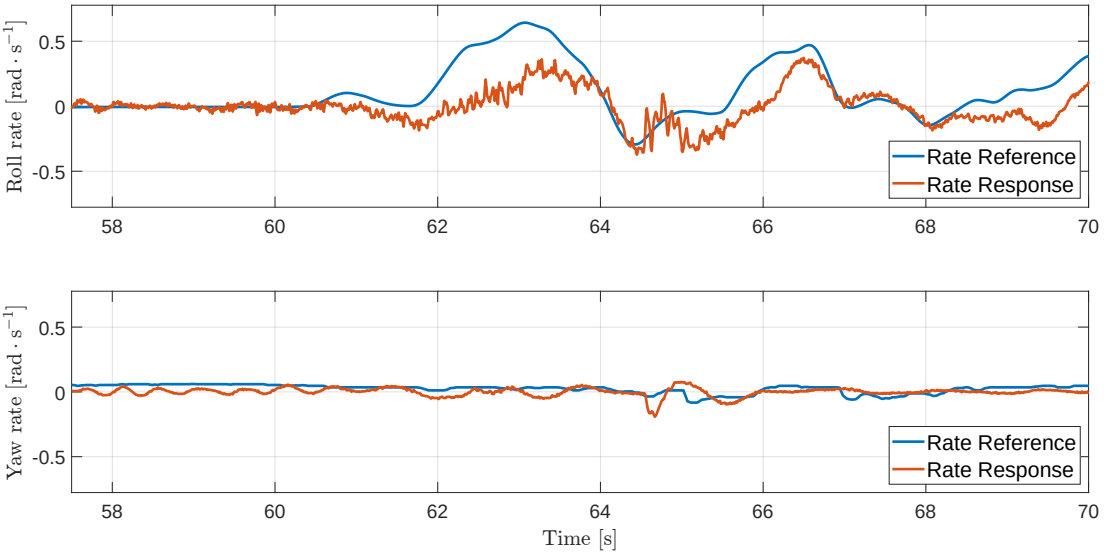

Figure 8.4. Roll and yaw rate response during pitch rate test.

The yaw rate was kept around zero during the entire maneuver and did not require significant pilot input. The same, however, can not be said about the roll rate controller.

Without the pilot input, it does not have sufficient bandwidth for effective disturbance rejection. Even then, the response was slower than expected.

Specific yaw and roll rate response tests were conducted to confirm these behaviors. The results are shown in Figures 8.5 and 8.6.

The yaw rate test has shown a good tracking performance. However, it also highlighted the system's tendency to oscillate during aggressive maneuvers.

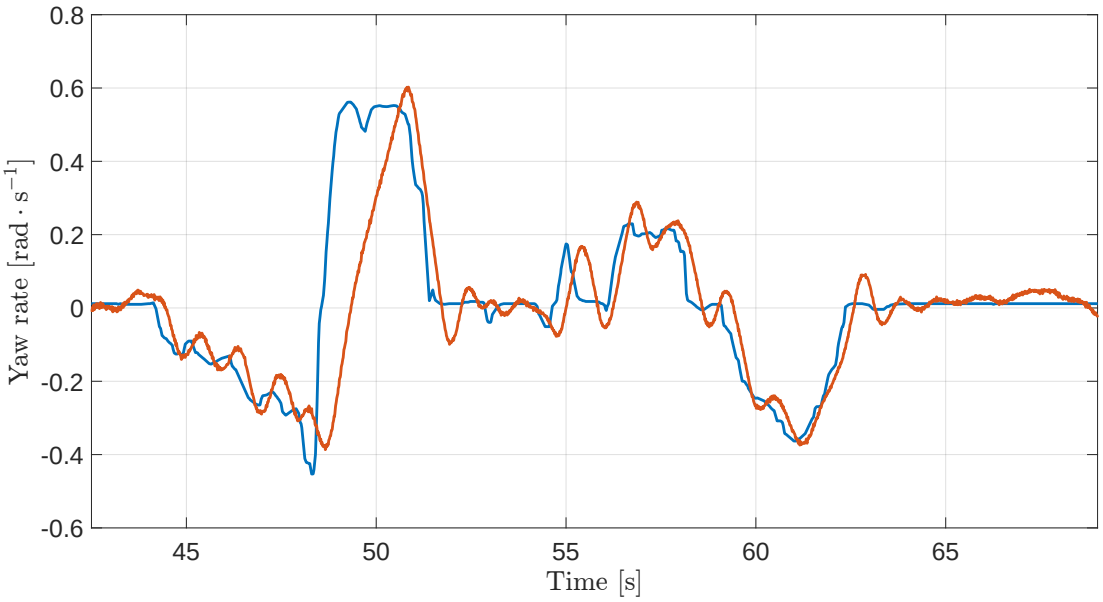

Figure 8.5. Yaw rate during low-speed maneuvering.

The roll rate test has shown a delay of up to 0.5 seconds between the pilot's input and the system's response. The system is stable and without significant oscillations. However, the phase delay is expected to cause oscillatory behavior of the attitude level controller.

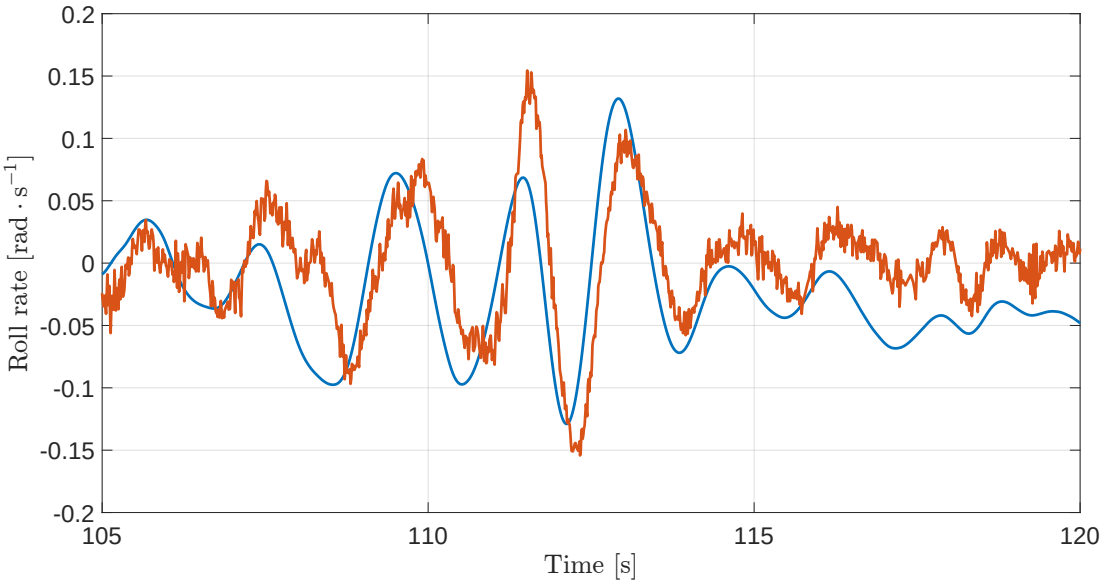

Figure 8.6. Roll rate test during low-speed maneuvering.

8.2 Attitude level validation.

The testing of rate level was followed by validation of the attitude level loop. The first test included several impulses in pitch attitude reference from the pilot during flight. The tracking of the required attitude is shown in Figure 8.7.

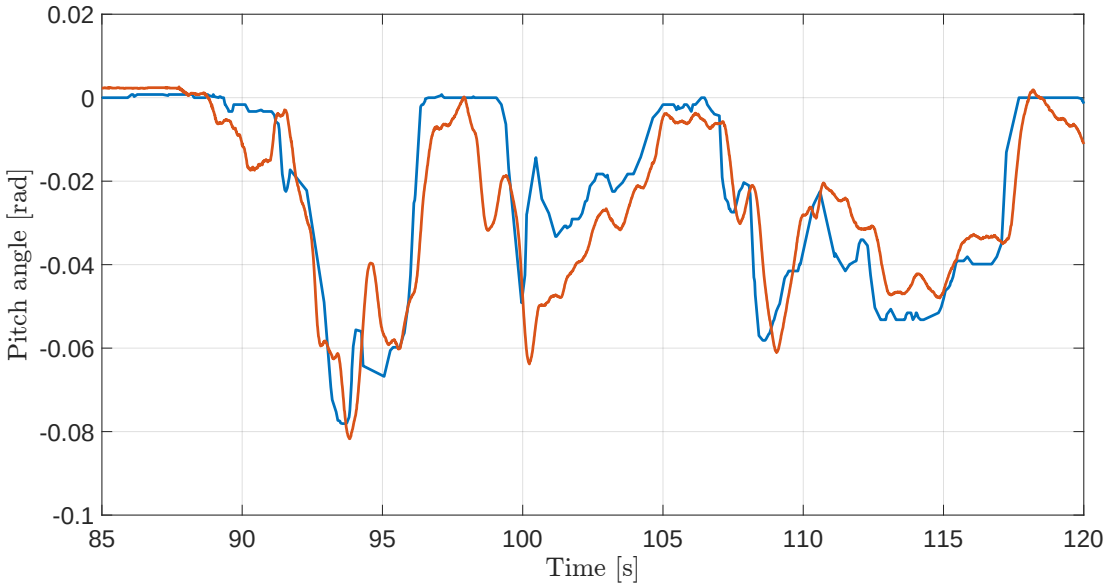

Figure 8.7. Pitch attitude controller test

The system shows sufficient capability to track the desired aircraft behavior. This is not surprising, as the rate level works well, so the attitude controller has to control relatively simple dynamics. This can not be said about the roll rate control loop. As the rate level has a significant delay and insufficient authority, the higher-level system can be expected to oscillate. This has been confirmed during tests of the roll attitude controller. Figure 8.8 shows the response to two impulse references.

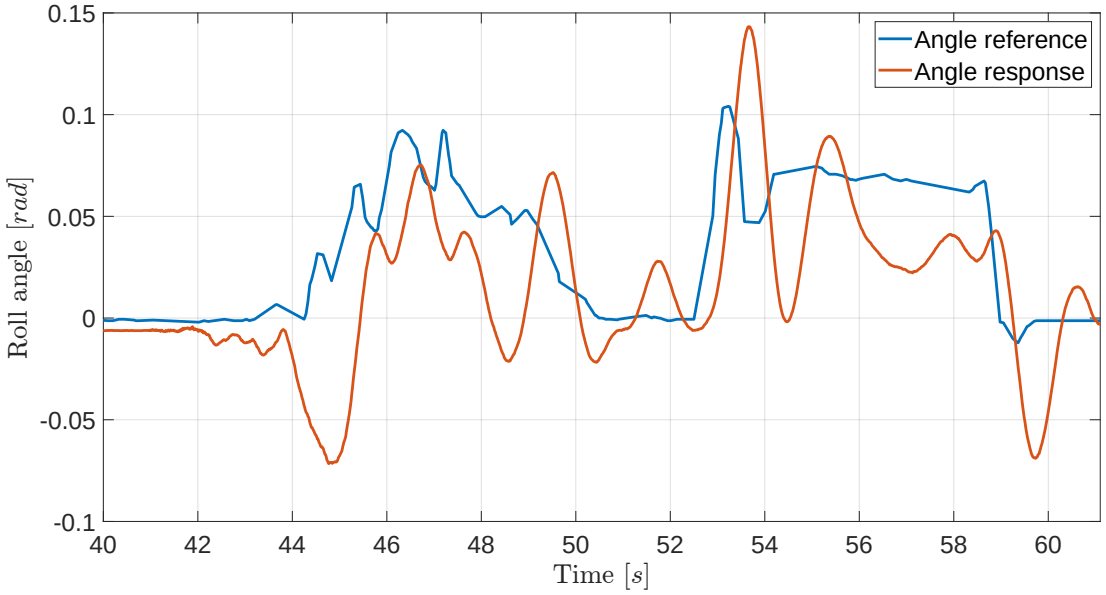

Figure 8.8. Roll attitude controller test.

Even though the system is stable and controllable, the dynamics show large oscillations, combined with significant overshoot and insufficient disturbance rejection. The

systems make the aircraft controllable. However, they are not able to sufficiently reduce the pilot workload. The controllers of the roll dynamics should be tuned during future flight tests to improve their behavior before more complicated control scenarios are tested.

8.3 Proposed roll control modifications

The roll rate controller's bandwidth can be increased by reducing or eliminating the band-stop filter, described in section 6.6. The change is justified by the fact, that the roll rate dynamics in flight do not exhibit significant oscillations at the natural frequencies of the wing. These frequencies have been measured during ground tests. Therefore, the measurements could be affected by the suspension or another part of the plane.

The elimination of the filter increases the bandwidth by itself but also allows for a gain increase of the CAS controller by 12 dB without reducing the system robustness.

The comparison between the original and modified setup is shown in Figure 8.9. The configurations were tested in simulations with external torque disturbance, represented by colored noise. The modified system reduces the roll rate error by a factor of two.

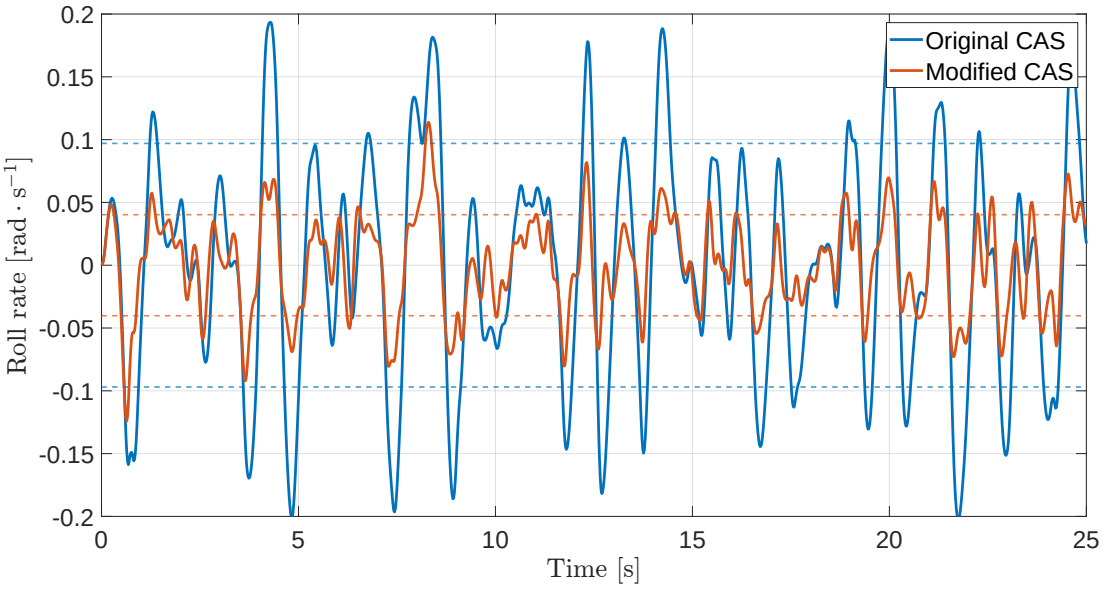

Figure 8.9. Comparison of disturbance rejection capabilities of the original and modified roll rate controllers. Dotted lines represent 1σ standard deviation.

8.4 Conclusion

The chapter described the first flight test of the drone system and validated rate and attitude level control in hover.

The pitch and yaw dynamics worked sufficiently well without further parameters tuning, which can be considered a success. Unfortunately, roll dynamics did not demonstrate sufficient control bandwidth and disturbance rejection. For this reason, more tests are needed to validate the controllability of the system in hover.

Many more flight tests are needed to validate the entire system. These tests can be expected to last at least several months to ensure safety and minimize the chance of a crash during testing. Therefore the main focus of the future work will be on extensive flight tests and validation of the results presented in this thesis.

Chapter 9
Results

The thesis successfully achieved all of its objectives, as proposed in section 1.3. An overview of the results is listed bellow

- Review of existing fly-by-wire solutions for VTOL aircraft, especially tilt-rotors, is summarized in Chapter 2. Two main approaches used to control tilt-rotor aircraft are described, including their advantages and disadvantages. This description motivated the development of a different control approach based on dynamics inversion and exact linearization algorithms.
- Non-linear mathematical model for the tilt-rotor aircraft was developed in Chapter 3. The model describes all essential aircraft sections necessary for fly-by-wire system design. The design neglects the interaction between propellers and the wing, which significantly simplifies the dynamics and allows to decouple aerodynamic surfaces and propellers inputs for attitude control. A modified η-V envelope for the VTOL system is presented to evaluate the aircraft's capabilities.
- Design of basic control architecture for the cruise regime is described in Chapter 4. The system uses dynamic inversion and hierarchical control approaches to simplify parameter tuning for individual control loops.
- Modifications of the cruise-specific system that allows for sub-stall speed control are presented in Chapter 5. The main difference in Mach and V_z hold systems is the introduction of an exact linearization control method for a smooth transition from hover to cruise.
- The developed fly-by-wire system was verified using simulations in Chapter 7 and actual flight tests of the VTOL drone model in Chapter 8. Simulations showed the system's capability to control the aircraft during all considered flight stages. Transition in complicated conditions, such as coordinated turns or climbs, was also demonstrated. External factors limited the number of flight tests, so only rate and attitude control in hover was verified. Even these limited results are significant, demonstrating the system's ability to control the existing drone system.

9.1 Future work

The main focus of future work will be on further flight testing, which is expected to last at least several months. Systems that were not verified in-flight are

- Mach and V_z hold systems
- Combination of aerodynamic surfaces and propellers based control in low-speed maneuvering
- Transition from hover to cruise in basic flight scenarios

Many of these tests would also benefit from an improved verification platform. For this reason, the second generation of drone aircraft will be developed. It is expected to include superior avionics, especially better airspeed measurement, and improved airframe stiffness.

Chapter 10
Conclusion

The fly-by-wire control system, developed for tilt-rotor VTOL aircraft, was presented in this thesis. The work builds on renewed development of VTOL aircraft, enabled by distributed electric propulsion and improved battery performance. The industry and academia are actively researching new strategies to control a VTOL plane with distributed propulsion. Even though several fly-by-wire architectures were already developed, each seems to have its specific issues.

Therefore, this thesis proposes a new design approach, based on exact linearization and dynamics inversion, that promises to be easily tunable, allow for a robust design approach, and be easy to test in an actual aircraft.

The entire design procedure was described in the thesis to demonstrate the system's use case and capabilities. It included the derivation of a specific mathematical model of tilt-rotor aircraft, followed by the generalized design of the fly-by-wire system. This theoretical part was followed by tuning the control parameters according to provided drone specifications. The parameterized system was finally verified in high fidelity simulations and basic flight tests, which were limited during the thesis's writing. The flight tests will continue in order to verify the entire control approach.

The simulation-based evaluation showed that the system can control the aircraft in all flight configurations. It also showed accurate tracking of the desired airspeed and climb rate. This means that the pilot's workload during VTOL flight should be comparable to flying general aviation aircraft.

References

[1] *XFV-1 experimental aircraft.* https://acesflyinghigh.files.wordpress.com/2014/05/xfv-1.jpg.

[2] Pavan, N. *Design of Tiltrotor VTOL and Development of Simulink Environment for Flight Simulations.*

[3] *Joby tilt-rotor prototype aircraft.* https://www.aerotime.aero/articles/30257-joby-air-taxi-prototype-crashes-during-testing#cover.

[4] *Wisk lift and thrust aircraft prototype.* https://www.bizjournals.com/sanjose/news/2019/12/03/boeing-kitty-hawk-reorganize-and-rebrand-mountain.html.

[5] *Dufour tilt-wing prototype aircraft.* https://evtol.com/news/dufour-evtol-initial-flight-testing/.

[6] Chen, Chao, Jiyang Zhang, Daibing Zhang, and Lincheng Shen. Control and flight test of a tilt-rotor unmanned aerial vehicle. *International Journal of Advanced Robotic Systems*. 2017-01-01, Vol. 14, No. 1. Available from DOI 10.1177/1729881416678141.

[7] Bacchini, Alessandro, and Enrico Cestino. Electric VTOL configurations comparison. *Aerospace*. Vol. 2019.

[8] Bauersfeld, L., and G. Ducard. Fused-PID Control for Tilt-Rotor VTOL Aircraft. *2020 28th Mediterranean Conference on Control and Automation (MED)*. IEEE, 2020, pp. 703-708. Available from DOI 10.1109/MED48518.2020.9183031.

[9] Oznalbant, Zafer, and Mehmet S. Kavsaoglu. Flight control and flight experiments of a tilt-propeller VTOL UAV. *Transactions of the Institute of Measurement and Control*. 2018, Vol. 40, No. 8, pp. 2454-2465. Available from DOI 10.1177/0142331218754618.

[10] Papachristos, Christos, Kostas Alexis, George Nikolakopoulos, and Anthony Tzes. Model predictive attitude control of an unmanned Tilt-Rotor aircraft. *2011 IEEE International Symposium on Industrial Electronics*. IEEE, 2011, pp. 922-927. Available from DOI 10.1109/ISIE.2011.5984282.

[11] Bauersfeld, L., L. Spannagl, G. Ducard, and C. Onder. MPC Flight Control for a Tilt-Rotor VTOL Aircraft. *IEEE Transactions on Aerospace and Electronic Systems*. 2021, Vol. 57, No. 4, pp. 2395-2409. Available from DOI 10.1109/TAES.2021.3061819.

[12] Allenspach, M, and GJJ Ducard. Nonlinear model predictive control and guidance for a propeller-tilting hybrid unmanned air vehicle.

[13] Rohr, David, Matthias Studiger, Thomas Stastny, Nicholas Nicholas R. J. Lawrance, and Roland Siegwart. Nonlinear Model Predictive Velocity Control of a VTOL Tiltwing UAV. *IEEE Robotics and Automation Letters*. 2021, Vol. 6, No. 3, pp. 5776-5783. Available from DOI 10.1109/LRA.2021.3084888.

[14] Escobar, Jossué Carino, Rogelio Lozano, and Moisés Bonilla Estrada. PVTOL control using feedback linearisation with dynamic extension. *International Journal of Control*. 2021-07-03, Vol. 94, No. 7, pp. 1794-1803. Available from DOI 10.1080/00207179.2019.1676468.

[15] Nemati, Alireza, and Manish Kumar. Non-Linear Control of Tilting-Quadcopter Using Feedback Linearization Based Motion Control. *Dynamic Systems and Control Conference*. American Society of Mechanical Engineers, 2014-10-22, Vol. 3. Available from DOI 10.1115/DSCC2014-6293.

[16] Belak, Jan, and Hanis Tomas. Decoupling of vehicle lateral dynamics using four-wheel steering system. *2021 23rd International Conference on Process Control (PC)*. IEEE, 2021-6-1, pp. 243-248. Available from DOI 10.1109/PC52310.2021.9447489.

[17] Singh, Rana Pratap. *Some Generalizations In Matrix Differentiation With Applications In Multivariate Analysis*.
`https://scholar.uwindsor.ca/etd/3531/`.

[18] *Airplane Parts and Functions*.
`https://www.grc.nasa.gov/www/k-12/airplane/airplane.html`.

[19] Gur, Ohad. Extending Blade-Element Model to Contra-Rotating Configuration. *IOP Conference Series: Materials Science and Engineering*. 2019-10-01, Vol. 638, No. 1, pp. 4, Figure 2. ISSN 1757-8981. Available from DOI 10.1088/1757-899X/638/1/012001.
`https://iopscience.iop.org/article/10.1088/1757-899X/638/1/012001`.

[20] Rostami, Mohsen, Joon Chung, and Daniel Neufeld. Vertical tail sizing of propeller-driven aircraft considering the asymmetric blade effect. *Proceedings of the Institution of Mechanical Engineers, Part G: Journal of Aerospace Engineering*. 2021. ISSN 0954-4100. Available from DOI 10.1177/09544100211029450.

[21] Alroqi, Abdurrhman, and Weiji Wang. Comparison of Aircraft Tire Wear with Initial Wheel Rotational Speed. *International Journal of Aviation, Aeronautics, and Aerospace*. 2015. Available from DOI 10.15394/ijaaa.2015.1043.

[22] Karnopp, Dean C., Donald L. Margolis, and Ronald C. Rosenberg. *Basic 2-port elements*.

[23] Panigrahi, Siddhant, Yenugu Siva Sai Krishna, and Asokan Thondiyath. Design, Analysis, and Testing of a Hybrid VTOL Tilt-Rotor UAV for Increased Endurance. *Sensors*. 2021, Vol. 21, No. 18. ISSN 1424-8220. Available from DOI 10.3390/s21185987.

[24] Liaqat, Saad Ali, Waleed Tahir, and Zaid Tahir. State Space System Modeling of a Quad Copter UAV. 2019.

[25] Stevens, Brian L., Frank L. Lewis, and Eric N. Johnson. *Controls Design, and Autonomous Systems*. Third edition ed. Wiley, 2016.

[26] Belák, Jan. *Advanced steering concept for overactuated vehicle*.

[27] Khalil, H.K. *Nonlinear Control*. Global edition ed. PEARSON, 2015.

[28] Gracey, William. The experimental determination of the moments of inertia of airplanes by a simplified compound-pendulum method. National aeronautics and space administration Washington DC, 1948.

[29] Doyle, John C. Guaranteed margins for LQG regulators. IEEE Transactions on automatic control, 1978.

Appendix A
Acronyms

CAS	Control augmentation systems
CG	Center of gravity
CS	Coordinate system
DOF	Degree of freedom
ESC	Electronic speed control
eVTOL	Electric vertical take-off and landing
FC	Flight computer
GPS	Global Positioning System
IMU	Inertial measurement unit (including 3-axis accelerometer and gyroscope)
LP	Low pass (filter)
LQG	Linear Quadratic Gaussian
LQR	Linear Quadratic Regulator
LTR	Loop transfer recovery
MC	Monte-Carlo
MIMO	Multiple input multiple output
MPC	Model predictive control
MTOW	Maximal take-off weight
NASA	National Aeronautics and Space Administration
PID	Proportional, Integral, Derivative
RC	Remote control
SAS	Stability augmentation systems
SIL	Software in the loop
VTOL	Vertical take-off and landing

Appendix B
Pendulum method

Figure B.1. Measurement of the drone's moments of inertia using the pendulum method.